Formation and Characterization of Mg-based Bulk Metallic Glasses and Nanocrystalline Materials

Thesis by

Wenshan Liu

In Partial Fulfillment of the Requirements

for the Degree of

Doctor of Philosophy

California Institute of Technology

Pasadena, California

1998

(Submitted June 25, 1997)

To my family

Acknowledgments

For my last five years at Caltech, I have found myself extremely lucky to be in such a great place and be with so many brilliant, nice and helpful people. I am grateful to them for playing an important role in my personal and professional life.

The most important one is my advisor, Prof. William L. Johnson. He has exceptional scientific intuition, enthusiasm and enjoyment of science. During the difficult and frustrating times of my research, he was always my unending source of inspiration, support and encouragement. I thank him for giving me the opportunity to pursue my Ph.D. at Caltech and for being a caring mentor.

My special thanks go to Carol Garland, our gifted microscopist. She helped me develop the skills for using electron microscopy. Lots of work done in this thesis would not be complete without her help, patience and willingness to share her immense practical knowledge.

I would like to thank many people in Keck lab for their friendship, cooperation in the lab and many discussions on various scientific and non-scientific topics, and I will apologize beforehand if I forget to mention anybody. They are Ralf Busch, Xianghong Lin, Uli Geyer, Susane Schneider, Mo Li, Jianzhong Li, Dale Conner, Richard Danliker, Andy Masuhr, Haein Chi-Yim, Mohit Jain and Pam Albertson.

The financial support from the Department of Energy under grant No. DE-FG03-86ER45242 is greatly appreciated.

Finally, I would like to express my deepest gratitude to my family. I would not be where I am today without the support of my family, especially my parents. I thank them for their unconditional love. I would also like to thank my lifelong partner Xiaomin who always stands by me at my worst and best times.

Abstract

The first metallic glass was discover by Duwez and his colleagues at Caltech in 1960. The recent development of new metallic alloys which form bulk metallic glasses at low cooling rates has led the metallic glasses research to significant advances. For the first time it has become possible to carry out measurements of thermophysical properties such as specific heat, viscosity, atomic diffusion, and crystal nucleation rates for liquid alloys over the full temperature range of the undercooled melt. These new materials exhibit a rich variety of phenomena, such as liquid/liquid phase separation and nanocrystalline phase formation, and have interesting potential as engineering materials.

This thesis reports the systematic studies of Mg-base amorphous, one of the best bulk metallic glass formers. The formation of coexistent amorphous and nanocrystalline phases in slowly quenched alloy of $Mg_{65-x}Cu_{25}Y_{10}Li_x$ containing 3 to 15 at.% of Li is reported. The grain size of the nanocrystal ranges from 2 to 20 nm increasing with Li content. The transmission electron microscopy investigations showed evidence of phase separation in $Mg_{62}Cu_{25}Y_{10}Li_3$ alloy. The thermodynamics and kinetics of $Mg_{65}Cu_{25}Y_{10}$ alloy were studied. Absolute values of specific heat capacities were measured with respect to sapphire standards for amorphous, crystal, superercooled liquid, and melt in differential scanning calorimetry. The differences in enthalpy, entropy and Gibbs free energy between crystal and superercooled liquid were calculated using the measured specific heat capacity and the heat of fusion. The

three-point beam-bending method was used to measure the viscosity of $Mg_{62}Cu_{25}Y_{10}Li_3$ alloy in amorphous and supercooled liquid using thermal mechanical analyzer. Strong glass behavior and glass forming ability were discussed. The phase separation and crystallization of the $Mg_{62}Cu_{25}Y_{10}Li_3$ alloy were studied with x-ray, differential scanning calorimetry, transmission electron microscopy, and small angle scattering. The results suggested that the decomposition in the undercooled liquid state triggers the crystallization as well as limits the crystal growth.

Contents

List of Figures

Chapter 1

Chapter 2

Chapter 3

Chapter 5

List of Tables

Chapter 1

Introduction

Metallic glasses were first obtained from liquid quenching by Duwez *et al.* [1] over thirty years ago in eutectic alloys of Au-Si and Pd-Si using rapid-quenching methods. Since then, metallic glass has been one of the focal points for scientific research. During the past several years, advances have been made in this field as a result of the discovery and development of several families of alloys with substantially improved glass forming ability. These new materials make it possible for the first time to carry out measurements of thermophysical properties such as specific heat, viscosity, atomic diffusion, and crystal nucleation rates for liquid alloys over the full temperature range of the undercooled melt. Also they exhibit a rich variety of phenomena such as liquid/liquid phase separation and nanocrystalline phase formation, and have interesting potential as engineering materials. This opens a broad field for science and application.

1.1 Definitions

A glass is defined as an amorphous solid which does not possess the long-rang order (periodicity) characteristic and which exhibits a glass transition. In simple words, a glass is a vitrified liquid, formed by continuous hardening of a cooled liquid. The hardening is determined quantitatively by viscosity and commonly we

define a solid as a material whose shear viscosity exceeds $10^{13.6}$ Ns/m^2 [2]. This rather arbitrary division of viscosity corresponds to a relaxation time of one day.

The absence of long-range order characteristic of an amorphous solid is most clearly evinced in a diffraction experiment such as x-ray diffraction (XRD) or transmission electron microscopy (TEM). For example using x-rays, one observes broad diffuse haloes instead of the sharp Bragg spots or rings produced by single crystal or polycrystalline samples. By only using diffraction pattern, a polycrystalline material which has a grain size below several nanometers may not be distinguishable from a glass.

The glass transition is the phenomenon in which a solid amorphous phase exhibits a more or less abrupt change in derivative thermodynamic properties such as heat capacity or thermal expansivity from crystal-like to liquid-like values with change of temperature. The glass transition can be measured using several different methods. One method is differential scanning calorimetry (DSC). Fig. 1.1 shows a typical heat capacity curve of a metallic glass [3]. The temperature in which the abrupt change of heat capacity occurs is called glass transition temperature, T_g. The glass transition temperature has different values for different heating rates. It has an onset and a completion value. With higher heating rates, the glass transition onset and completion temperatures are shifted to higher values. T_g can also be related to the viscosity and be defined as the temperature at which the viscosity has a value of 10^{13} poise. Fig. 1.2 shows the viscosities of a variety of glass-forming systems as a function of temperature [4].

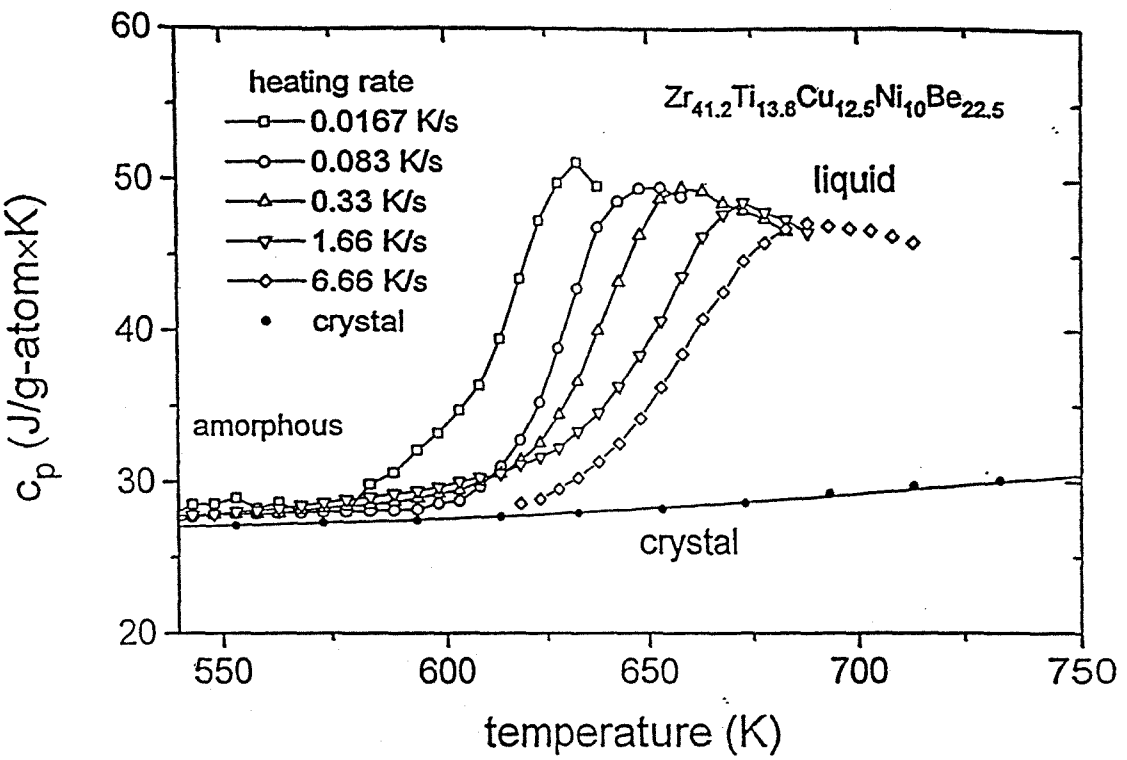

Fig. 1.1 Specific heat capacity as a function of temperature for different heating rates as measured by Differential Scanning Calorimetry (DSC) for a glassy $Zr_{41.2}Ti_{13.8}Cu_{12.5}Ni1_0Be_{22.5}$ alloy. Reproduced from ref. 3.

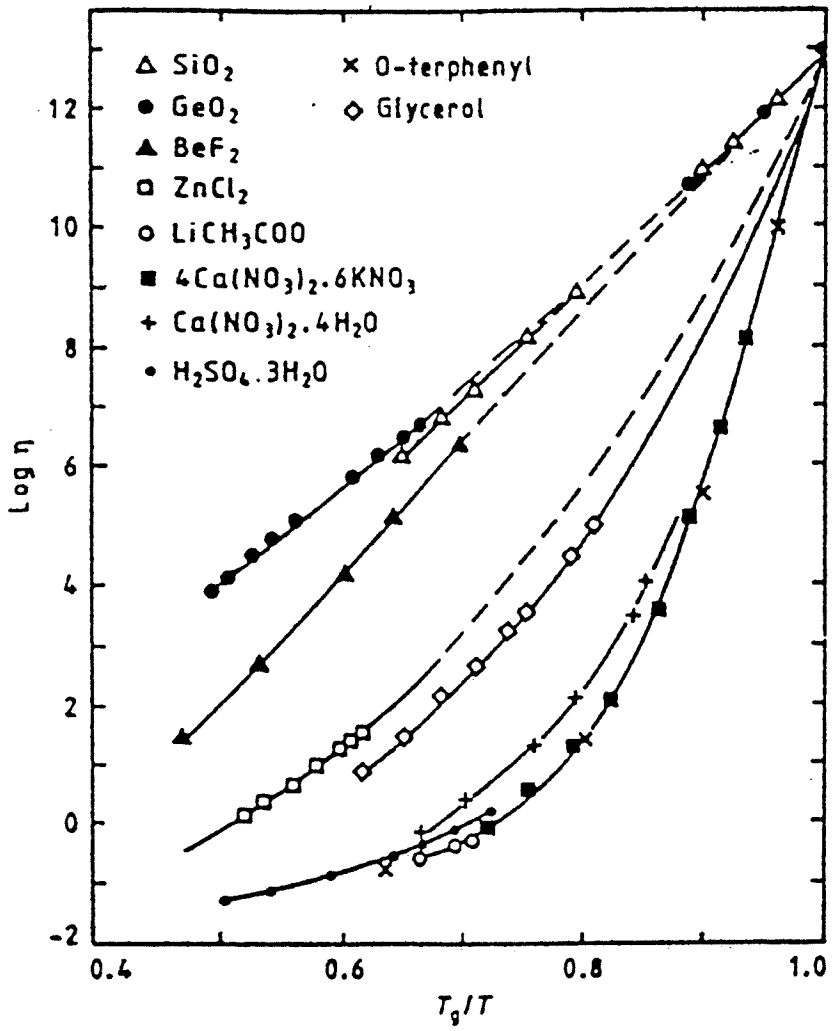

Fig. 1.2 Viscosities of a variety of glass-forming systems as a function of reduced reciprocal temperature. The curves have been normalized such that the glass-transition temperature is defined to be when $\eta=10^{13}$ poise. Reproduced from ref. 4.

Polycrystalline materials of the grain size less than 25 nm are called nanocrystalline materials. These materials are structurally disordered in comparison with a single crystal but exhibit periodic atomic order on a length scale of several nanometers. Hence, they demonstrate quite different physical properties from both the conventional polycrystalline materials and amorphous materials. Nanocrystalline materials are characterized by their small crystallite-size in the range of a few nanometers which are separated by high-angle grain or interphase boundaries and, consequently, by their large volume fraction of disordered regions, the grain boundaries. Sometimes the distinction between an amorphous structure and a nanocrystalline structure becomes difficult.

1.2 Glass formation vs. crystallization

A glass is not in the lowest-energy state and it will crystallize at high enough temperature and/or given long enough time. This means that a glass is a metastable phase compared to corresponding equilibrium crystalline phases. A metastable phase is a non-equilibrium phase of matter for which the evolution toward the equilibrium phase is suppressed by a kinetic barrier. At sufficiently low temperature, the critical fluctuation required to overcome the kinetic barrier and form the equilibium phase may be so improbable that the metastable phase becomes "stable" on any practical timescale.

The most common method to obtain glasses is quenching from melt. Liquid metals may often be undercooled well below melting point T_m without crystallization occurring. For sufficiently deep undercooling, the liquid may undergo a glass transition at T_g and becomes a glass. To produce the glass, the liquid must pass through the undercooled regime ($T_g<T<T_m$) rapidly enough to avoid the occurrence of critical crystal nucleation events. The kinetic requirement to suppress the crystallization can be generally expressed as a minimum (critical) cooling rate R_c.

A liquid becomes thermodynamically unstable with respect to the crystal when it is cooled below melting point. The free energy difference between liquid and crystal phase provides a driving force for crystallization. However, the creation of the liquid-crystal interface disfavors the nucleation process since it contains a positive interfacial energy. According to classical homogeneous nucleation theory by Turnbull [5, 6], the free energy change associated with the existing spherical crystalline embryos is given by:

$$\Delta G = 4\pi\, r^2\sigma + \frac{4\pi}{3} r^3 \Delta G_v . \qquad (1.1)$$

As shown in Fig. 1.3, σ ($\sigma>0$) is the liquid-crystal interfacial energy per unit area. ΔG_v is the free energy difference between liquid and crystal per unit volume. It can be estimated as:

$$\Delta G_v = \Delta S_f (T_m - T) - \int_{Tm}^{T} dT' \int_{Tm}^{T'} \frac{\Delta C_p}{T''} dT'' . \qquad (1.2)$$

The competition of these two terms gives a free energy maximum:

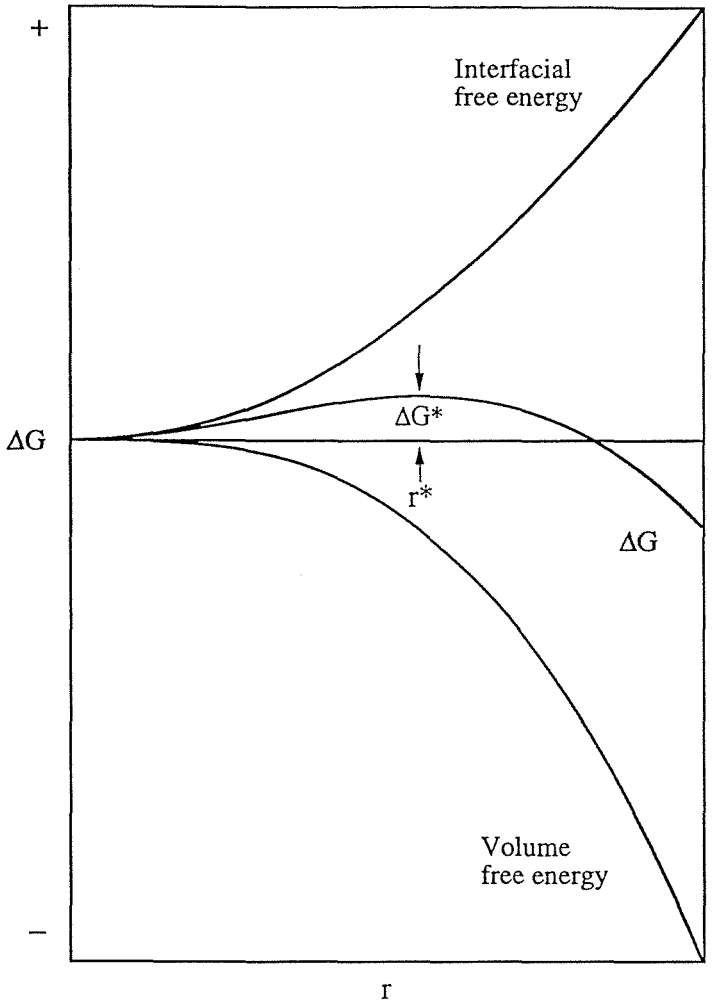

Fig. 1.3 Gibbs free energy associated with the nucleation of a crystalline embryo as a function of its radius.

$$\Delta G^* = \frac{16\pi}{3}\left(\frac{\sigma^3}{\Delta G_v}\right) \tag{1.3}$$

at a critical nucleus radius:

$$r^* = -\frac{2\sigma}{\Delta G_v} \ . \tag{1.4}$$

Crystalline nuclei larger than r* will grow while those smaller than r* will tend to remelt. ΔG* is the activation energy for nucleation. This Turnbull model was developed for pure elements or for the polymorphic case which assumes that the crystals forming have the same composition as the liquid.

For the small embryos to grow, atoms need to transport from the liquid side of the interface to the crystal side so that the embryos growth rate is determined by the rate of atom transport which is described by the atomic diffusivity D. The diffusivity is related to the viscosity by the Stokes-Einstein relation:

$$D = \frac{kT}{3\pi a_o \eta} \ , \tag{1.5}$$

where a_o is the interatomic distance, k is Boltzmann constant.

Therefore, the homogeneous nucleation rate contains two parts, one comes from the free energy difference between liquid and crystal, the other from the atomic mobility. It is given by:

$$I = \frac{k_n}{\eta(T)} \exp\left(-\frac{\Delta G^*}{kT}\right), \tag{1.6}$$

where k_n is a kinetic constant. The viscosity of undercooled melts has been found to be well described by the Vogel-Fulcher equation:

$$\eta(T) = A\exp(\frac{B}{T - T_o}). \tag{1.7}$$

Using the linear approximation, the expression for ΔG becomes:

$$\Delta G = -\frac{L\Delta T_r}{V_m}, \tag{1.8}$$

and the homogeneous nucleation frequency becomes:

$$I = \frac{K_n}{\eta(T)}\exp(-\frac{16\pi}{3}\frac{\alpha^3\beta}{\Delta T_r^2 T_r}), \tag{1.9}$$

where L is the molar latent heat of fusion, V_m is molar volume of the crystal, T_r is the reduced temperature T/T_m, $\Delta T_r = 1-T_r$, α and β are dimensionless parameters as:

$$\alpha = \frac{(N_A V_m^2)^{1/3}\sigma}{L}; \qquad \beta = \frac{L}{RT_m}, \tag{1.10}$$

where N_A is Avogardro's number.

With empirical data, Turnbull obtained the homogeneous nucleation frequency as a function of reduced temperature [7], shown in Fig. 1.4. One sees that for $t_g<1/2$, the maximum nucleation rate will be so large to make glass formation impossible in practical sense, while for $t_g>2/3$, the rates of the nucleation of crystals should become very small at all temperatures which in turn results in the formation of bulk metallic glasses.

The above arguments only consider homogeneous nucleation. However, in practice, heterogeneous nucleation is also involved and occurs at container walls and on foreign particles which catalyze the nucleation.

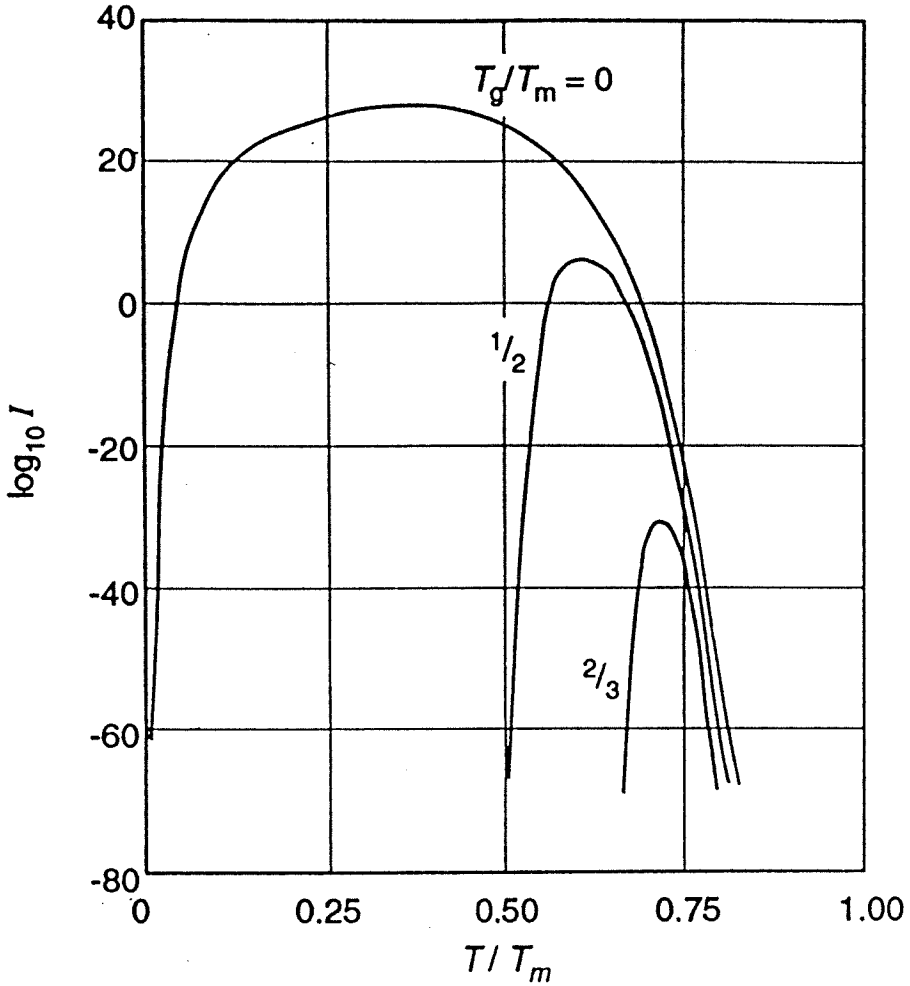

Fig. 1.4 The logarithm (base 10) of the nucleation frequency (in nuclei/cm^{3}s) as a function of reduced temperature T/T_m for various values of the reduced glass transition temperature $t_g=T_g/T_m$. Reproduced from ref. 7.

1.3 Glass forming systems

Metallic glass alloys were first obtained by Duwez *et al.* [1] by liquid quenching in eutectic alloys of Au-Si and Pd-Si using rapid-quenching methods with cooling rates of 10^5-10^6 K/s. Cohen and Turnbull suggested that the formation of the these metallic glasses is connected with the occurrence of a deep eutectic feature in the corresponding phase diagrams. They pointed out that since T_g is in general found to be a slowly varying function of composition, the reduced glass transition temperature t_g exhibits a maximum vs. composition near deep eutectics and hence it is relatively easier to bypass the nucleation during quenching at such compositions.

Since this early work, a wide variety of metallic glasses have been discovered. These metallic glasses have different properties from corresponding crystalline materials. For example, metallic glasses have very high elastic limit, high hardness, very high strength, good bend ductility, better soft magnetic properties, increased corrosion resistance, low coefficient of friction and other useful properties [8, 9]. But the requirement of very high cooling rate at 10^5-10^6 K/s limits production of these metallic glasses to thin foils and ribbons having a maximum thickness less than 100 μm. For a long time the only exception was the Ni-Pd-P alloy system where bulk glassy material with thickness up to 1 cm could be produced at low cooling rates by fluxing the surface to avoid heterogeneous nucleation of crystals [10, 11].

Starting from early 1990's, several bulk metallic glass systems were found by Inoue, Masumoto *et al.* At Tohoku University in Japan by judicious choice of the

compositions in multicomponent alloy systems, such as La-Ni-Al [12], Mg-Cu-Y [13] and Zr-Cu-Ni-Al [14]. These systems have critical cooling rates of 10^2 K/s for glass formation and exhibit good thermal stability above the glass transition. The Inoue group reported making fully amorphous samples up to several millimeters thick. Here, we define a bulk metallic glass as having a minimum dimension of 1 mm which is equivalent to a critical cooling rate of about 10^3 to 10^4 K/s.

More recently, alloys with critical cooling rates of 10 K/s and even as low as 1 K/s have been found. One of the best is Zr-Ti-Cu-Ni-Be discovered by Peker and Johnson at Caltech [15]. This system forms amorphous samples with a smallest dimension of several centimeters. This has opened new opportunities for industrial applications, as well as fundamental studies of the undercooled liquid state, glass transition and crystallization. But the toxicity of beryllium is an unforunate drawback for some practical applications. Later, Lin and Johnson at Caltech found some new bulk metallic glasses such as Ti-Zr-Cu-Ni [16] and Zr-Ti-(Nb)-Cu-Ni-Al [17] which can make amorphous samples near 1 cm. Fig. 1.5 shows the critical cooling rates for glass formation and corresponding maximum thickness of some metallic glasses.

The development of new metallic alloys which form bulk glasses at low cooling rates has led to significant advances in the study of undercooled liquid metals and the glass transition in metallic systems. An unexpected result, from studies on the crystallization in the new bulk glass forming alloys, has been the recognition that crystallization is frequently preceded by phase separation of the undercooled liquid into two liquid phases of different composition.

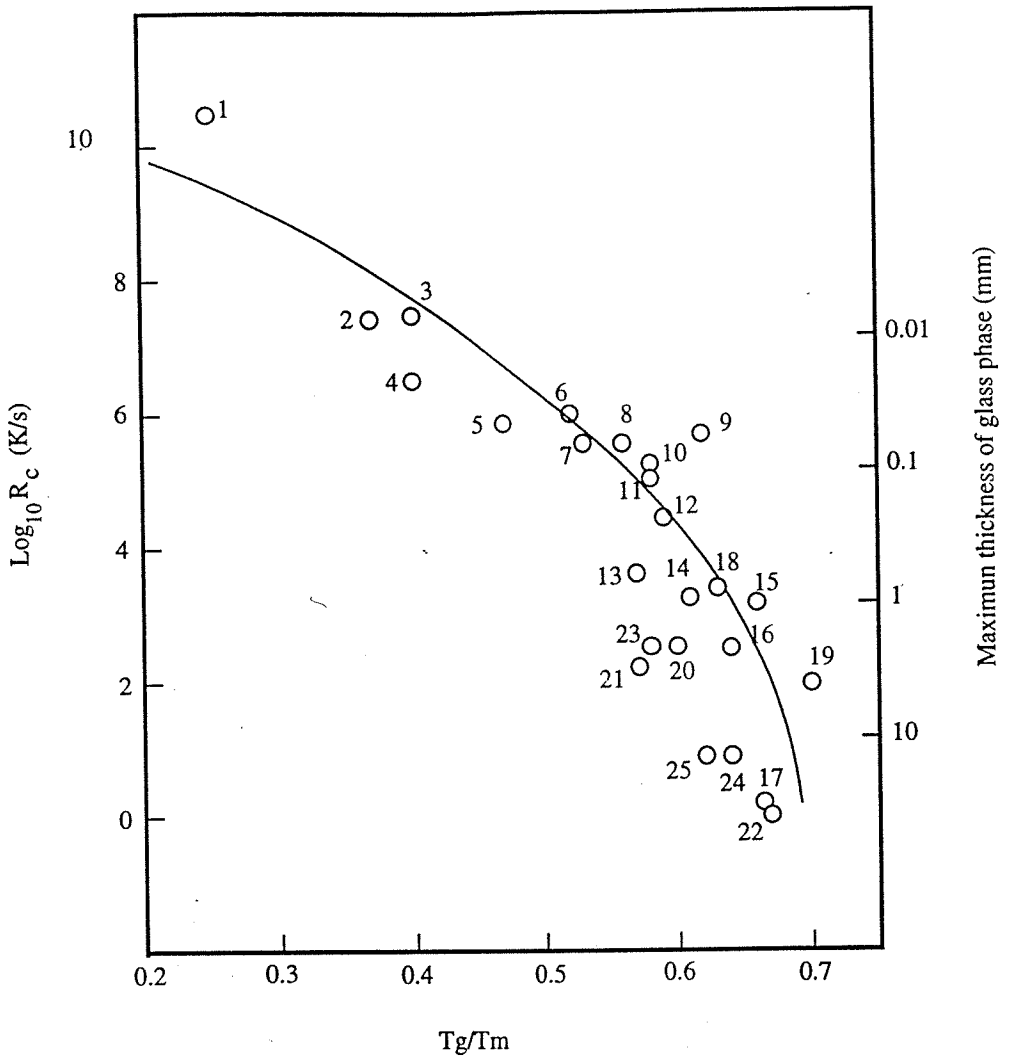

Fig. 1.5 Critical cooling rates for glass formation and corresponding maximum thickness of glass phases. Key to the alloys: (1)Ni; (2)$Fe_{91}B_9$; (3)$Fe_{89}B_{11}$; (4)Te; (5)$Au_{77.8}Ge_{13.8}Si_{8.4}$; (6)$Fe_{83}B_{17}$; (7)$Fe_{41.5}Ni_{41.5}B_{17}$; (8)$Co_{75}Si_{15}B_{10}$; (9)Ge; (10)$Fe_{79}Si_{10}B_{11}$; (11)$Ni_{75}Si_8B_{17}$; (12)$Fe_{80}P_{13}C_7$; (13)$Pt_{60}Ni_{15}P_{25}$; (14)$Pd_{82}Si_{18}$; (15)$Ni_{62.4}Nb_{37.6}$; (16)$Pd_{77.5}Cu_6Si_{16.5}$; (17)$Pd_{40}Ni_{40}P_{20}$; (18)$Au_{55}Pb_{22.5}Sb_{22.5}$; (19)$La_{55}Al_{25}Ni_{10}Cu_{10}$; (20)$Mg_{65}Cu_{25}Y_{10}$; (21)$Zr_{65}Cu_{17.5}Ni_{10}Al_{7.5}$; (22)$Zr_{41.2}Ti_{13.8}Cu_{12.5}Ni_{10}Be_{22.5}$; (23)$Ti_{34}Zr_{11}Cu_{47}Ni_8$; (24)$Zr_{52.5}Ti_5Cu_{17.9}Ni_{14.6}Al_{10}$; (25)$Zr_{57}Nb_5Cu_{15.4}Ni_{12.6}Al_{10}$. Reproduced from ref. 17.

REFERENCES

[1] W. Klement IV, R. H. Willens, and P. Duwez, Nature, **187**, 869 (1960).

[2] S. R. Elliott, *Physics of Amorphous Materials*, (Longman Group Ld., London and New York, 1983), p5.

[3] R. Busch, Y. J. Kim, and W. L. Johnson, J. Appl. Phys., **77**, 4039 (1995).

[4] C. A. Angell and W. Sichina, Ann. NY Acad. Sci., **279**, 53 (1976).

[5] J. H. Holloman, and D. Turnbull, Prog. In Met. Phys. **4**, 333 (1953).

[6] D. Turnbull, *Solid State Physics*, Vol. **3**, (Academic Press, New York, 1956).

[7] D. Turnbull, Contemp. Phys., **10**, 473 (1969).

[8] H. H. Liebermann (ed.), *Rapidly Solidified alloys: Processes, Structures, Properties, Applications*, (Marcel Dekker Inc., New York, 1993).

[9] F. E. Luborsky (ed.), *Amorphous Metallic Alloys*, (Butterworth, London, 1983).

[10] A. J. Drehman and A. L. Greer, Acta Metall., **32**, 323 (1984).

[11] H. W. Kui, A. L. Greer, and T. Turbull, Appl. Phys. Lett., **45**, 615 (1984).

[12] A. Inoue, K. Kita, T. Zhang, and T. Masumoto, Mater. Trans., JIM, **30**, 722 (1989).

[13] A. Inoue, A. Kato, T. Zhang, S. G. Kim, and T. Masumoto, Mater. Trans., JIM, **32**, 609 (1991).

[14] T. Zhang, A. Inoue, and T. Masumoto, J. Mat. Sci. Lett., **12**, 700 (1993).

[15] A. Peker, and W. L. Johnson, Appl. Phys. Lett., **63**, 2342 (1993).

[16] X. H. Lin, and W. L. Johnson, J. Appl. Phys., **78**(11), 6514 (1995).

[17] X. H. Lin, and W. L. Johnson, unpublished results.

[18] Ph.D. thesis of X. H. Lin, Caltech.

Chapter 2

Formation of Mg-Cu-Y-Li bulk metallic glasses and nanocrystalline alloys

2.1 Introduction

Mg-based metallic glasses have attracted increasing interest because they possess high strength and are light weight. Binary systems Mg-Zn [1] and Mg-Cu [2] were found to be able to form amorphous many years ago using rapidly solidified techniques. Around 1990, Inoue and Masumoto *et al.* at Tohoku University in Japan found several families of Mg-based metallic glasses by melt spinning which have a cooling rate of about 10^6 K/s [3, 4, 5]. Table 2.1 summarizes some Mg-based glass-forming alloy systems by melt spinning [6]. The Mg-Ln-TM amorphous alloys have a wide supercooled liquid region before crystallization as well as a large glass-forming ability. Also, they have high tensile fracture strength and high corrosion resistance. The highest tensile fracture strength in the Mg-Ln-TM amorphous reaches 830 MPa, which is about twice as high as that for conventional Mg-based crystalline alloys. Among these systems, Mg-Cu(Ni)-Y is the best glass former. Bulk metallic glasses have been produced by metal mold-casting. For the best alloy $Mg_{65}Cu_{25}Y_{10}$, fully glassy rods with a diameter of 7 mm were obtained by high-pressure die-casting.

Table 2.1 Mg-based amorphous alloys produced by single-roller melt-spinning, Ln = lanthanide metal; TM = transition metal (Ni, Cu, Zn).

Alloy component	Metal-metal system	Metal-metalloid system
Binary	Mg-Ca, Mg-Ni, Mg-Cu, Mg-Zn, Mg-Y	
Ternary	Mg-Ca-Al, Mg-Ca-Li, Mg-Ca-TM, Mg-Sr-TM, Mg-Al-Ln, Mg-Al-Zn, Mg-Ni-Ln, Mg-Cu-Ln, Mg-Zn-Ln	Mg-Ca-Si, Mg-Ca-Ge, Mg-Ni-Si, Mg-Ni-Ge, Mg-Cu-Si, Mg-Cu-Ge, Mg-Zn-Si, Mg-Zn-Ge,

In the past few years, several systems have been reported that exhibit coexistent nanocrystalline and amorphous phases, such as fcc-Ni in Ni-Si-B [7], fcc-Al in Al-Ni-Ce [8], hcp-Mg in Mg-Zn-La [9] and Mg-Zn-Ce [10], and hcp-Co in Co-Zr-B [11]. These nanocrystalline and amorphous coexistent systems exhibit very different physical properties from both conventional crystalline materials and fully amorphous materials. For example, in Al-Ln-TM ternary system, the mixed phases alloys with nanoscaled fcc-Al embedded in an amorphous matrix exhibit excellent mechanical strength which is about two times of those amorphous single phase alloys. But all of the above systems were formed using rapid cooling techniques like

splat-quenching or melt-spinning. The thickness of these samples is below 50 μm, and the estimated cooling rate is about 10^6 K/s. Such nanoscale amorphous structures have not been generally found when lower cooling rates are used. In this chapter, I will present studies of the formation of bcc nanocrystals in amorphous matrix at relatively low cooling rates when a few percent of Li is added to Mg-Cu-Y system.

2.2 Experiment

Mg-Cu-Y-Li ingots were alloyed by induction melting a mixture of the elements of purity ranging from 99.9% to 99.999% on a water-cooled silver boat under a Ti-gettered argon atmosphere. The ingots were repeatedly turned over and remelted to ensure homogeneity. Then they were further remelted under vacuum in a quartz tube using a rf induction coil and then injected in a copper mold under argon at about 1 atm pressure. Fig. 2.1 illustrates the schematic of the mold-casting apparatus. The copper mold has strip shaped cavities of about 2 cm length, 4-6 mm width, and various thickness from several hundred μm to several mm. The typical samples used here are strips with 1 mm thickness. The structure of the strips was examined by x-ray diffraction using a 120° position sensitive detector (Inel) and a collimated Co-Kα radiation (λ=1.790 Å). Thermal properties, including the glass transition, crystallization and melting behavior, were measured by using a Perkin-Elmer differential scanning calorimeter (DSC4) interfaced to a personal computer for data processing and analysis. The samples were contained in molybdenum pans

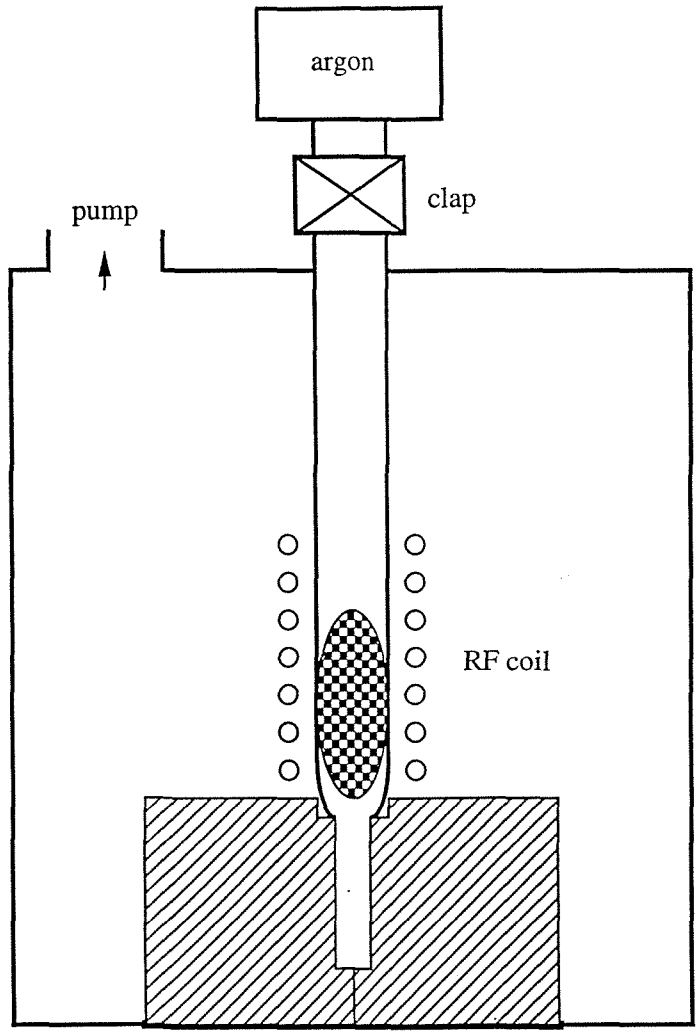

Fig. 2.1 Schematic of the mold-casting setup.

and scanned in a flowing argon atmosphere to reduce oxidation. Vicker's hardness of the material was obtained using a Leitz micro hardness tester. Microstructural characterization was performed by a Philips TEM430 operating at 300 KV.

2.3 Results and discussions

2.3.1 Formation

Fig. 2.2 shows the x-ray diffraction patterns of the surfaces of as-cast $Mg_{65}Cu_{25}Y_{10}$ and $Mg_{65-x}Cu_{25}Y_{10}Li_x$ (x=3, 6, 8, 10, and 15 at. %) strip samples with a fixed thickness of 1 mm. It is clear that the alloys with Li content higher than 6% are partially amorphous and partially crystalline. The $Mg_{50}Li_{15}Cu_{25}Y_{10}$ sample has a complex structure containing several crystalline phases while $Mg_{57}Li_8Cu_{25}Y_{10}$ and $Mg_{55}Li_{10}Cu_{25}Y_{10}$ contain only one simple crystal phase identified as simple bcc-Mg_7Li_3 (one atom per unit cell) with lattice constant a=3.52 Å. The grain size of the bcc phase increases with increasing Li content. We can estimate the grain size of particles by full-width at half maximum of diffraction peaks using the formula:

$$L = \frac{0.94\lambda}{(\Delta 2\theta)\cos\theta}, \qquad (2.1)$$

and the estimated grain size is about 10 to 20 nm. The x-ray patterns taken from interior cross-sectioned surfaces of the samples are the same as those taken from exterior surfaces. This implies that the bcc nanocrystalline phase is nucleated not only on external surfaces but also throughout the bulk samples, *i.e.*, it is nucleated

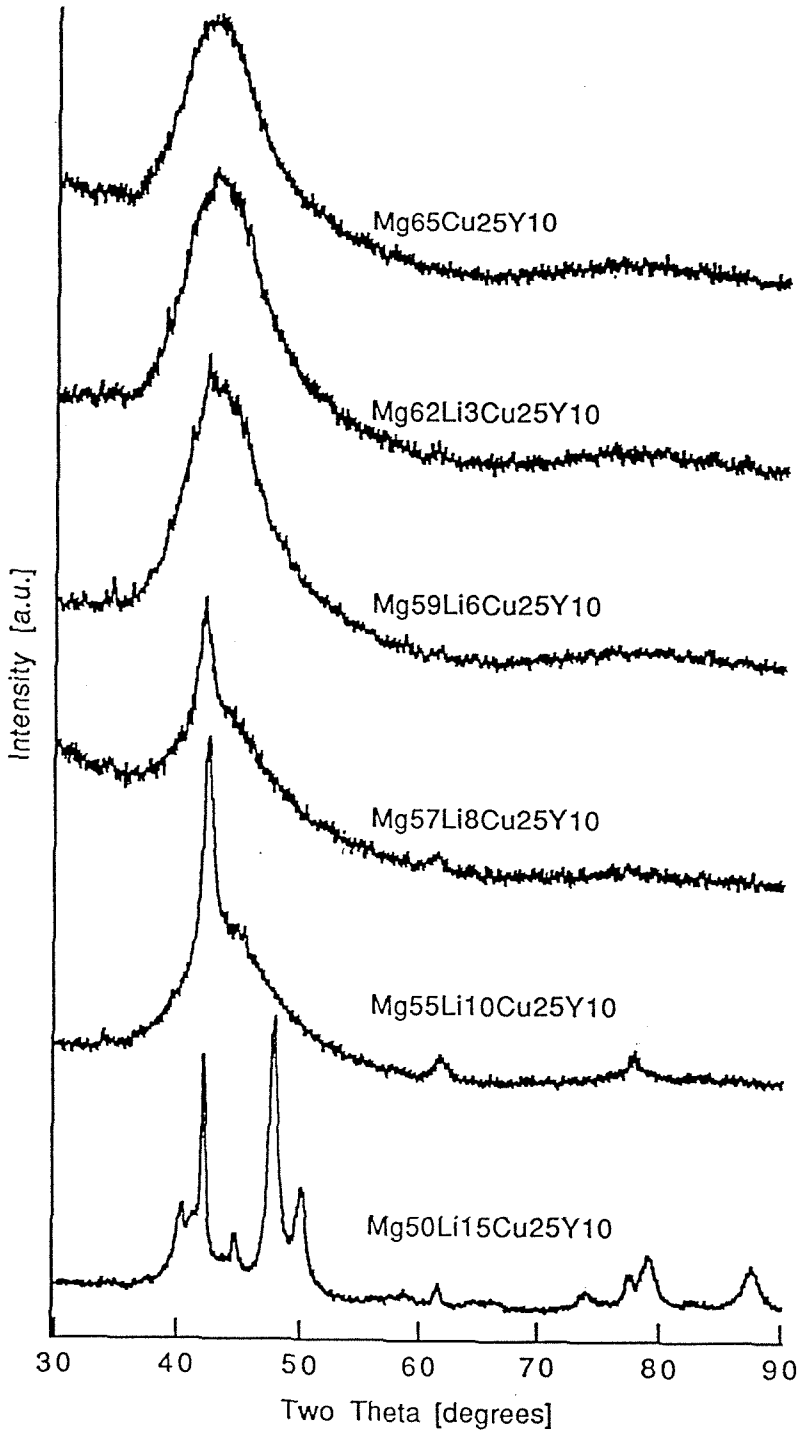

Fig. 2.2 X-ray diffraction patterns of as-cast strips of 1 mm thickness for $Mg_{65}Cu_{25}Y_{10}$ and $Mg_{65-x}Cu_{25}Y_{10}Li_x$ (x=3, 6, 8, 10, and 15 at. %).

uniformly throughout the sample. It is also observed that the relative intensity of the diffraction peaks corresponding to bcc nanocrystalline Mg_7Li_3 phase increases as the Li content increases. This indicates that the amount of bcc-Mg_7Li_3 phase increases with increasing Li content. The fact that the bcc-Mg_7Li_3 phase is still found in $Mg_{50}Li_{15}Cu_{25}Y_{10}$ means this phase is relatively stable. This can also be seen in the x-ray diffraction patterns of $Mg_{59}Li_6Cu_{25}Y_{10}$ samples which were heated to 170 °C or 230 °C in a DSC at a heating rate of 20 K/min and then subsequently cooled to ambient temperature as shown in Fig. 2.3. The peaks showing in the x-ray pattern for $Mg_{59}Li_6Cu_{25}Y_{10}$ sample annealed up to 170 °C correspond to bcc-Mg_7Li_3, while those in the sample annealed up to 230 °C are mixture of Mg_7Li_3 and Mg_2Cu phases.The alloys with 3 or 6% Li look fully amorphous by x-ray diffraction. But from the selected area diffraction patterns and dark-field TEM images of these alloys shown in Fig. 2.4, one can see that there are ultrafine nanocrystals distributed uniformly throughout the amorphous matrix. The crystallite sizes range from 2 to 6 nm. From statistics, the average of the grain size is approximate 3 nm. Table 2.2 lists the estimated grain sizes of the $Mg_{65-x}Cu_{25}Y_{10}Li_x$ alloys, from TEM or x-ray diffraction patterns.

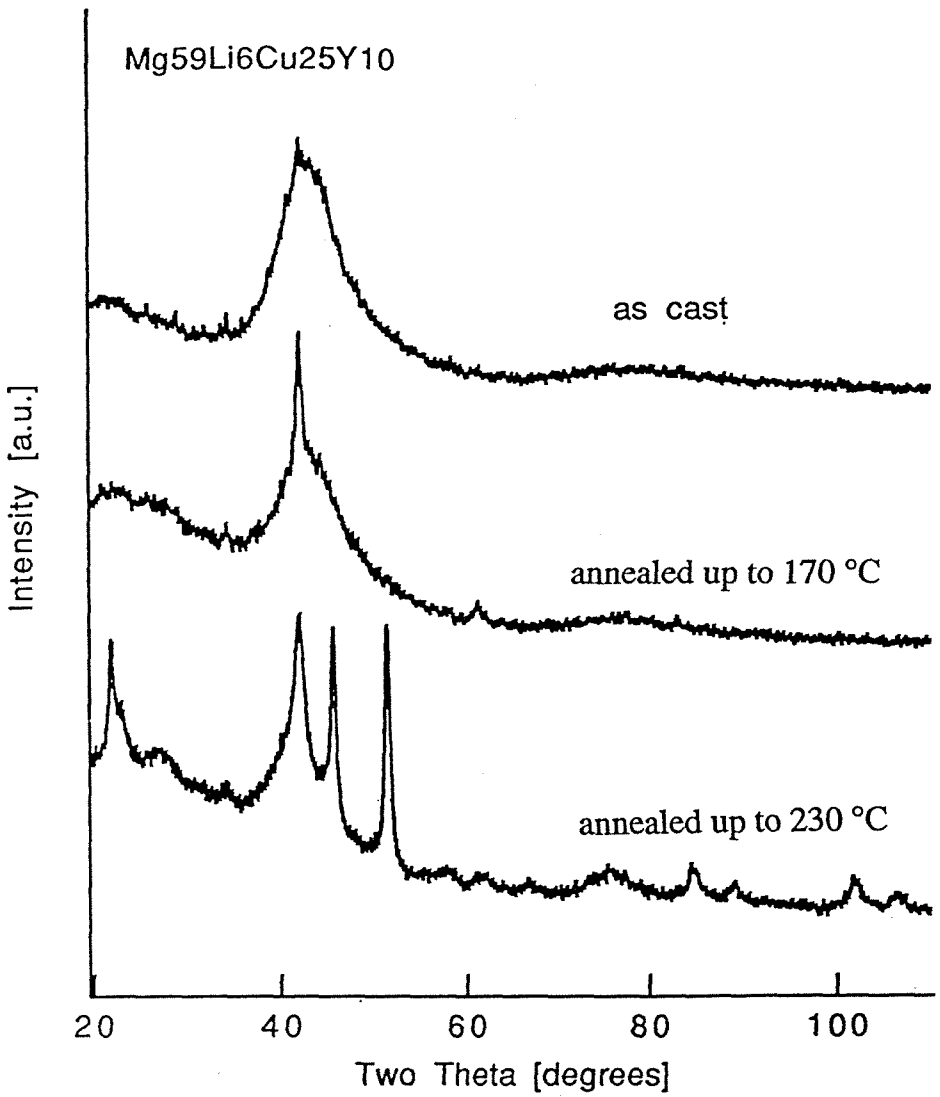

Fig. 2.3 X-ray diffraction patterns of $Mg_{59}Li_6Cu_{25}Y_{10}$ in the as-cast state and in samples heated to 170 °C or 230 °C, respectively, in a DSC at a heating rate of 20 K/min and then subsequently cooled to ambient temperature.

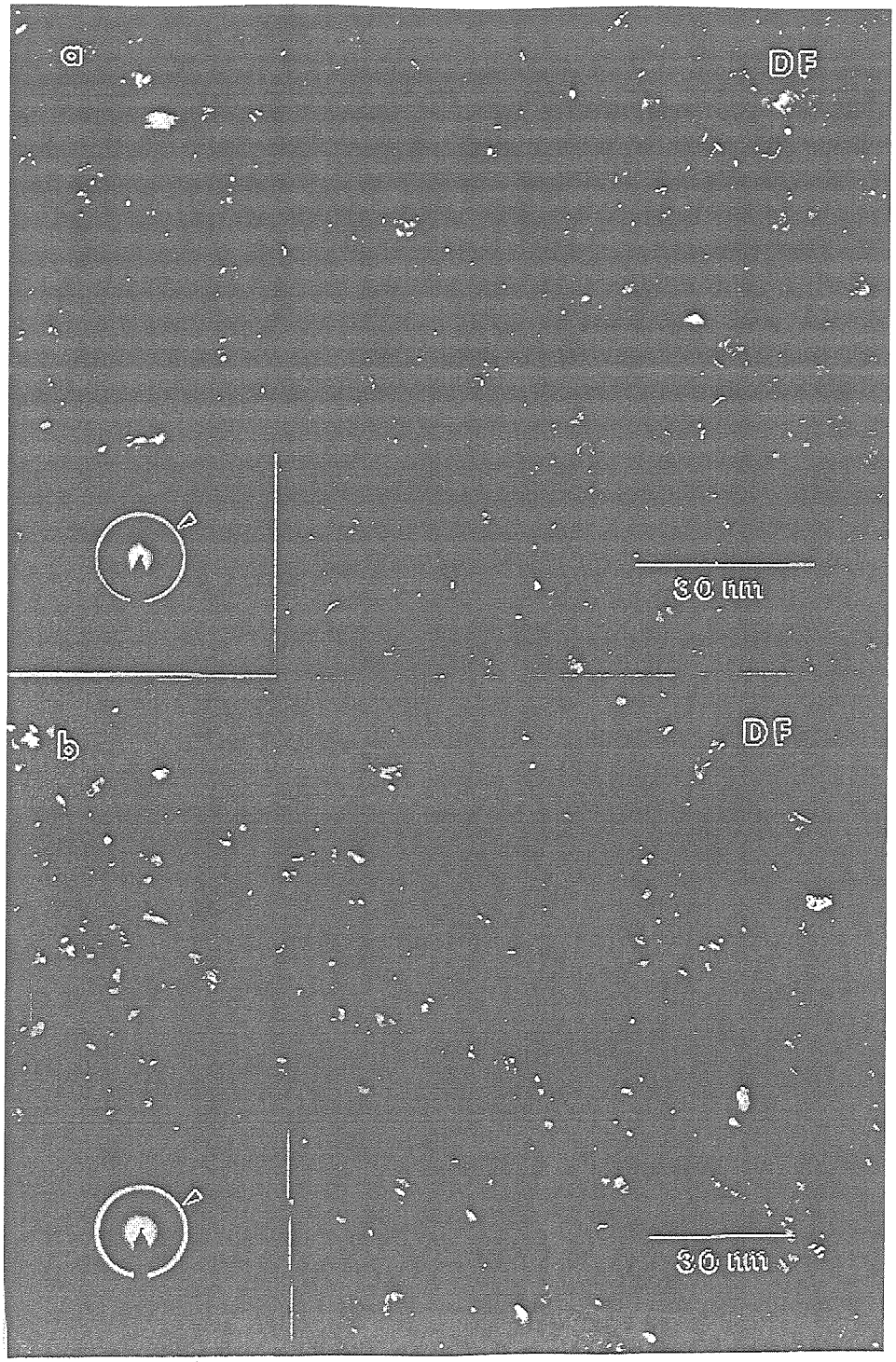

Fig. 2.4 TEM images of (a)$Mg_{62}Cu_{25}Y_{10}Li_3$ and (b)$Mg_{59}Cu_{25}Y_{10}Li_6$.

Table 2.2 The estimated grain sizes of the $Mg_{65-x}Cu_{25}Y_{10}Li_x$ alloys, from TEM or x-ray diffraction patterns.

Li (at. %)	grain size (nm)
3	3.2
6	3.4
8	10
10	14

2.3.2 Thermal analysis

DSC traces at various compositions for $Mg_{65-x}Cu_{25}Y_{10}Li_x$ (x=3, 6, 8, 10, and 15) taken using a heating rate of 10 K/min are shown in Fig. 2.5. Two exothermic peaks are observed in the scan of $Mg_{59}Cu_{25}Y_{10}Li_6$ beginning at 141 °C and 208 °C, respectively. It was confirmed from the x-ray diffraction patterns for annealed samples shown in Fig. 2.3 that the first peak was due to precipitation and grain growth of the nanoscale bcc-Mg_7Li_3 while the second one was due to the transformation of the remaining amorphous matrix to the intermetallic phase Mg_2Cu. The glass transition endotherm and crystallization exotherm to bcc-Mg_7Li_3 are overlapping in other scans. One also notes that the total heat release for crystallization of bcc-Mg_7Li_3 phase is relatively small, estimated to be about 90 cal/mole. This means the free energy difference between the purely amorphous phase

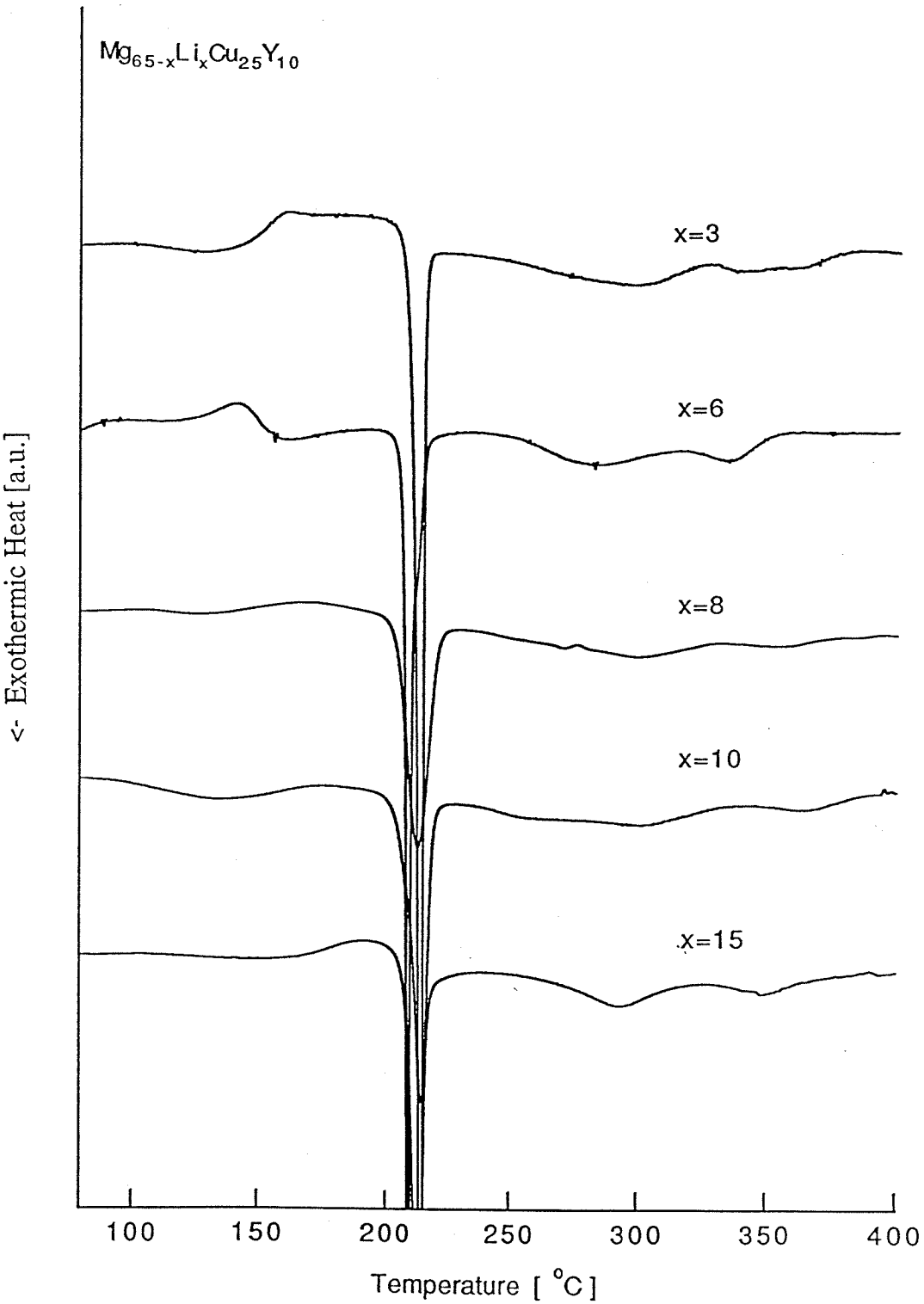

Fig. 2.5 DSC scans for as-cast $Mg_{65-x}Cu_{25}Y_{10}Li_x$ (x=3, 6, 8, 10, and 15) at a heating rate of 10 K/min.

and the partially crystallized nanocrystalline phase is small, suggesting that the driving force for nanoscale precipitation of the bcc-Mg_7Li_3 phase is also small.

Fig. 2.6 shows a comparison of DSC scans for $Mg_{65-x}Cu_{25}Y_{10}Li_x$ (x=6, 8, and 10) in the as-cast state (solid line) to the state previously annealed at 170 °C to crystallize Mg_7Li_3 (dash line) with a heating rate of 10 K/min. In the scans for the annealed Mg-Cu-Y-Li, the T_g of the amorphous matrix increases with both annealing and increasing Li content. It is known [12] that T_g tends to increase with an increase of magnitude and number of the attractive bonds among the constituent atoms. As the volume fraction of the bcc-Mg_7Li_3 phase increases, one expects the Cu and Y contents of the remaining amorphous matrix to increase. In the amorphous Mg-Cu-Y system, both increasing Cu and Y content will result in an increase of T_g [5]. Also, after annealing, the crystallization temperature, T_x, for Mg_2Cu decreases since the remaining amorphous has been enriched in copper due to the precipitation of Mg_7Li_3.

The thermal behavior of $Mg_{65-x}Cu_{25}Y_{10}Li_x$ alloys near the melting temperature is shown in Fig. 2.7. $Mg_{62}Cu_{25}Y_{10}Li_3$ shows a relatively sharp melting endotherm while $Mg_{50}Cu_{25}Y_{10}Li_{15}$ has a more complicated melting structure exhibiting a series of exotherms. The latter alloy starts to melt at a solidus temperature of 433 °C followed by complete melting at liquidus temperature 495 °C. Table 2.3 summarizes the thermal parameters including the glass transition temperature, T_g, the crystallization temperature, T_x, for Mg_2Cu, the total heat of crystallization, ΔH_x, the melting temperature, T_m, and the latent heat, Lm, where T_g, T_x, and T_m are defined as

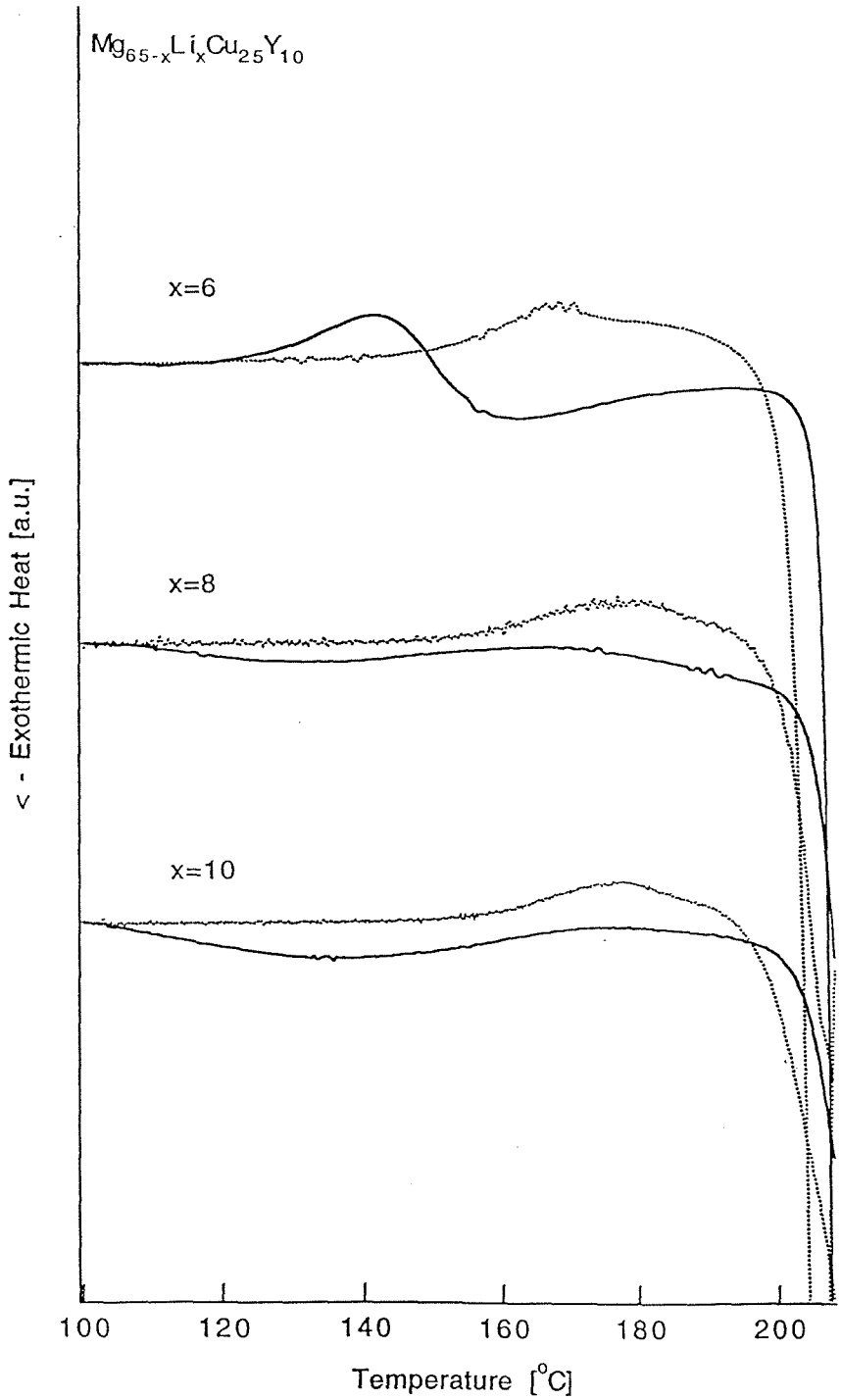

Fig. 2.6 DSC scans for $Mg_{65-x}Cu_{25}Y_{10}Li_x$ (x=6, 8, and 10) in the as-cast state (solid line) and previously heated up to at 170 °C to crystallize Mg_7Li_3 (dash line) with a heating rate of 10 K/min.

the onset points of corresponding events. In the case of melting, both the solidus and liquidus temperatures are given.

Table 2.3 Thermal parameters for $Mg_{65-x}Cu_{25}Y_{10}Li_x$ (x=3, 6, 8, 10, and 15) alloys. The data were measured from DSC scans with heating rate of 10 K/min. T_g is the glass transition temperature of amorphous matrix. T_x is crystallization temperature of Mg_2Cu. ΔH_x is the heat of crystallization. T_m^{sol} is the solidus temperature, T_m^{liq} is the liquidus temperature, and L_m is latent heat. Vicker's hardness H_v of some samples are also shown.

Li (at.%)	T_g (°C)	T_x (°C)	ΔH_x (cal/mol)	T_m^{sol} (°C)	T_m^{liq} (°C)	L_m (cal/mol)	H_v (Kg/mm^2)
3	141	214	708	454	472	2051	290
6	150	208	385	433	460	1961	302
8	154	205	336	433	464	1768	---
10	155	204	288	434	476	1777	---
15	---	210	361	433	495	1537	---

2.3.3 Mechanical property

Vicker's hardness measurements on these alloys were carried out. The typical accuracy of the measurement was 3%. The value for $Mg_{65}Cu_{25}Y_{10}$ alloy is H_v=269 Kg/mm^2. Using the well known relation $H_v=3\sigma_y$ [13], the yield strength of this

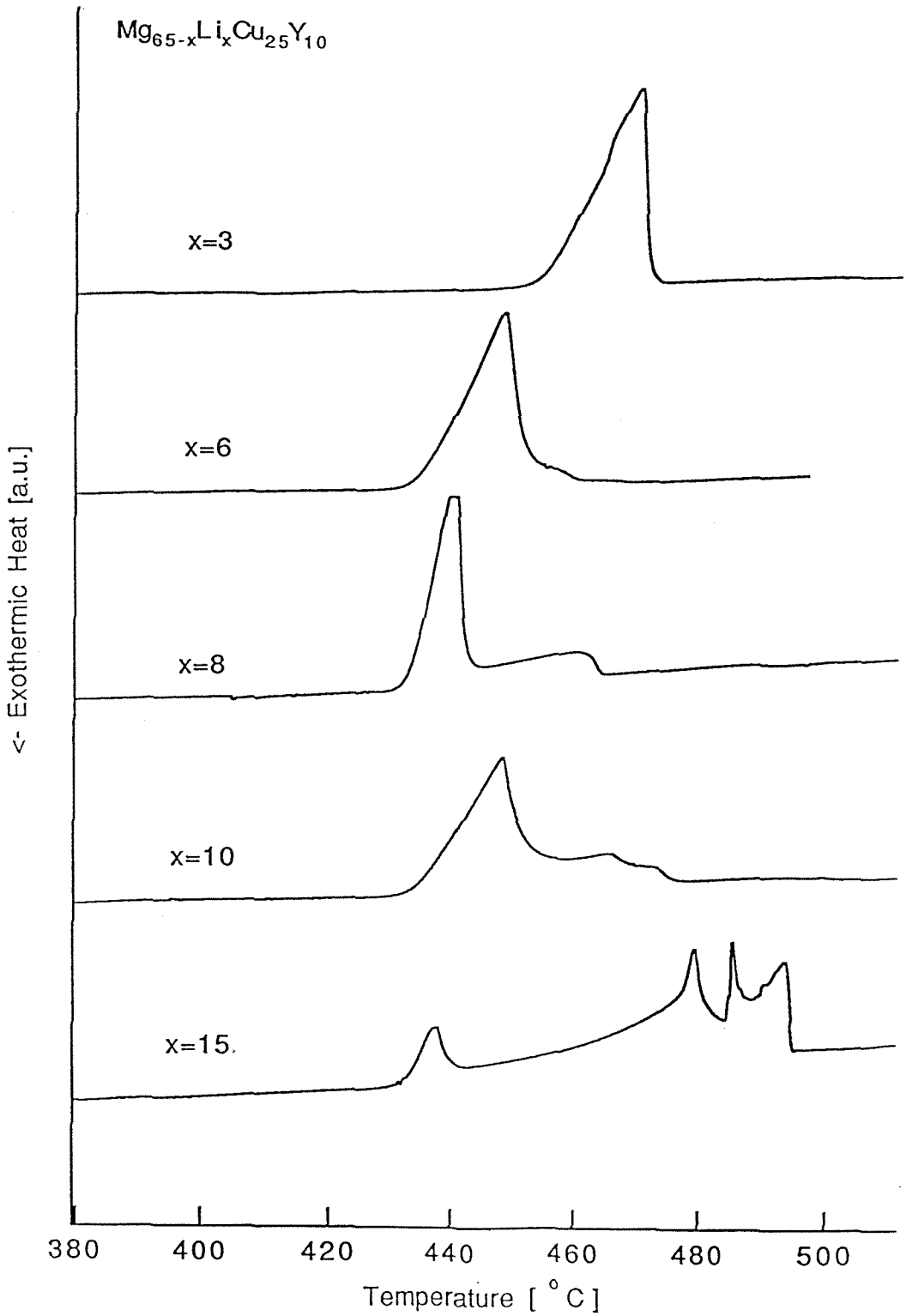

Fig. 2.7 DSC scans for as-cast $Mg_{65-x}Cu_{25}Y_{10}Li_x$ (x=3, 6, 8, 10, and 15) alloys near the melting point with a heating rate of 10 K/min.

amorphous alloy is approximately 900 MPa. The values for $Mg_{62}Cu_{25}Y_{10}Li_3$ and $Mg_{59}Cu_{25}Y_{10}Li_6$ are 290 and 302 Kg/mm^2, respectively. Here we can see the increasing of the mechanical strength with dispersion of nanoscale particles.

2.3.4 Phase separation

Fig. 2.8 shows the high resolution electron micrograph for as-cast $Mg_{62}Cu_{25}Y_{10}Li_3$. There is an obvious contrast in the TEM image which suggests two apparently different amorphous regions in the image. These amorphous domains are separated by a relatively sharp boundary. Based on these images, we suggest that the amorphous alloy has undergone phase separation during undercooling and solidification. The domains that exhibit lighter contrast appear to be fully amorphous. On the other hand, one observes well-developed groups of crystalline lattice fringes in regions contained within the darker domains. These fringes can be identified with the bcc nanocrystalline phase. The overall amorphous domain sizes are about 10 nm while the grain size of the nanocrystalline is smaller. Since the nanocrystalline phase is bcc-Mg_7Li_3, this suggests that the darker regions are Mg-Li rich, while the lighter regions are Mg-Li poor. It appears that phase separation occurs in the liquid state prior to crystallization of the nanophase during cooling from the melt. Nucleation of the bcc nanophase then occurs preferentially in the Mg-Li-rich amorphous phase. The subsequent growth of these Mg-Li-rich nanocrystals would then be restricted by the size of the phase-separated domains in which they nucleated. Thus, the phase separation acts both to trigger the nucleation and to limit the growth

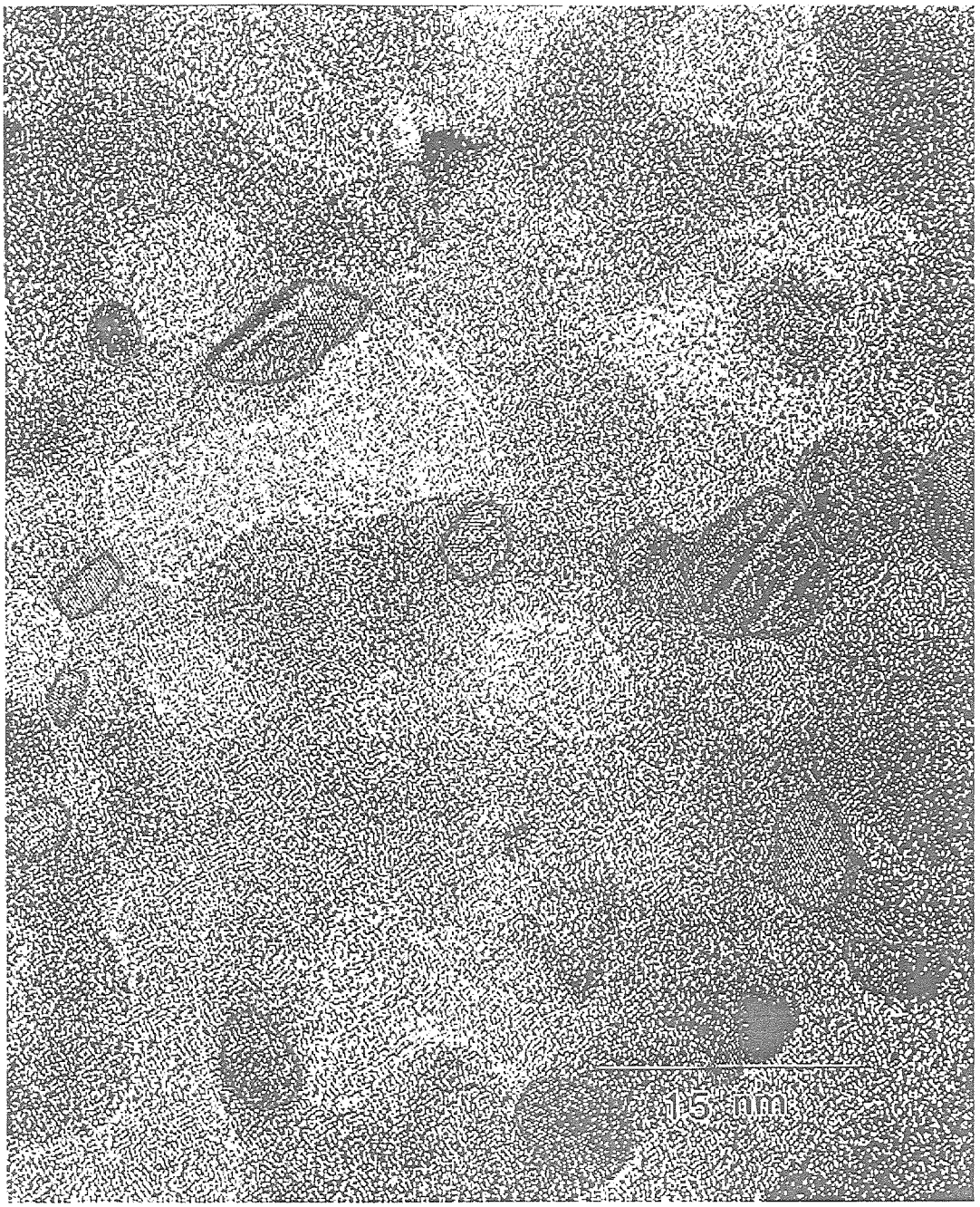

Fig. 2.8 The high resolution electron micrograph for as-cast $Mg_{62}Cu_{25}Y_{10}Li_3$. The particles with crystal fringes are indicated.

of the Mg_7Li_3 crystals. Further investigation and analysis of the phase separation and crystallization of this alloy will be discussed in Chapter 5.

2.4 Conclusion

It is found that a nanoscale intermetallic phase bcc-Mg_7Li_3 with a grain size of 2 to 20 nm is formed by nucleation in the bulk amorphous $Mg_{65-x}Cu_{25}Y_{10}Li_x$ system. The nanocrystalline particles are homogeneously distributed throughout the bulk sample. The ratio of nanocrystal to amorphous phase and the grain size of the nanocrystalline both increase as Li content increases. Adding Li changes the structure of Mg-Li-Cu-Y alloys from bulk amorphous to amorphous plus nanocrystalline, then finally to a mixture of several intermetallic phases. From high resolution TEM images, we suggest that $Mg_{62}Cu_{25}Y_{10}Li_3$ undergoes phase separation during cooling in the liquid state and forms two phases that are, respectively, Mg-Li rich and Mg-Li poor with a characteristic length scale of about 10 nm. The primary crystallization occurs in the Mg-Li-rich regions, and the crystallines are restricted to nanometer size because the boundaries of the two amorphous regions constrain the growth of the crystals. It has been found that the presence of Li plays an important role in the formation of nanoscale bcc structure.

REFERENCES

[1] A. Calka, M. Madhava, D. E. Polk, B. B. Giessen, H. Matyja, and J. V. Sande, Scr. Metall., **11**, 65 (1970).

[2] F. Sommer, G. Bucher, and B. Fredel, J. Phys. C, **41**, 563 (1980).

[3] A. Inoue, K. Ohtera, K. Kita, and T. Masumoto, Jpn. J. Appl. Phys., **27**, L2248 (1988).

[4] A. Inoue, M. Kohinata, K. Ohtera, A. P. Tsai, and T. Masumoto, Mater. Trans., JIM, **30**, 378 (1989).

[5] S. G. Kim, A. Inoue, and T. Masumoto, Mater. Trans., JIM, **31**(11), 929 (1990).

[6] A. Inoue and T. Masumoto, Mater. Sci. Eng. A, **173**, 1 (1993).

[7] A. Inoue, T.Shibata, and T. Masumoto, Mater. Tran., JIM, **33**(5), 491 (1992).

[8] A. Inoue, Y. H. Kim, and T. Masumoto, Mater. Tran., JIM, **33**(5), 487 (1992).

[9] A. Inoue, N. Nishiyama, S. G. Kim, and T. Masumoto, Mater. Tran., JIM, **33**(4), 360 (1992).

[10] S. G. Kim, A. Inoue, and T. Masumoto, Mater. Tran., JIM, **32**(9), 875 (1991).

[11] H. Kimura, A. Inoue, Y.Murakami, and T. Masumoto, Sci. R. Tok. A, **36**(2), 213 (1992).

[12] H. S. Chen, Rep. Prog. Phys., **3**, 353 (1980).

[13] L. A. Davis, *Mechanical Behavior of Rapidly Solidified Materials*, edited by S. M. L. Sastry and B. A. MacDonald, (the Metallurgical Society, Inc., 1986).

Chapter 3

Thermodynamics and Kinetics of $Mg_{65}Cu_{25}Y_{10}$ bulk metallic glass

3.1 Introduction

During the past several years, new families of multicomponent glass forming alloys such as La-Al-Ni [1], Zr-Ni-Al-Cu [2], Mg-Cu-Y [3], and Zr-Ti-Cu-Ni-Be [4] have been found which exhibit very good glass forming ability. These bulk metallic glasses show high thermal stability and have a large supercooled liquid region when heated above the glass transition temperature. This makes it possible for detailed studies of the thermophysical properties of metallic melts in the whole undercooled liquid region. The thermophysical properties include specific heat capacity, viscosity, diffusion, surface tension, and thermal expansion coefficient. For the Zr-Ti-Cu-Ni-Be system, some thermophysical properties have been measured far into the supercooled region, such as heat capacity [5], viscosity [6], diffusion [7] and emissivity [8].

In this chapter, we focus on thermodynamics and kinetics of the $Mg_{65}Cu_{25}Y_{10}$ alloy, which is one of the best bulk glass formers known so far. The heat capacity was measured in a differential scanning calorimeter (DSC). The viscosity measurements were done in a thermal mechanical analyzer (TMA). The kinetics and

thermodynamics in the supercooled liquid will be compared and discussed in the framework of the fragility concept. Furthermore, the knowledge of the specific heat capacity of the undercooled liquid as well as the crystalline state enables us to determine enthalpy, entropy and Gibbs free energy of the undercooled liquid with respect to the crystal as a function of temperature. One reason that we choose $Mg_{65}Cu_{25}Y_{10}$ is that it has relatively low melting point, which is about 723 K, so that we can measure its heat capacity all the way up to its melt point and above, in a single DSC. Thus, we can get very consistent data with less errors.

3.2 Thermodynamics

3.2.1 Experimental methods

$Mg_{65}Cu_{25}Y_{10}$ ingots were prepared from a mixture of elements of purity ranging from 99.9% to 99.999% by induction melting on a water-cooled silver boat under a Ti-gettered argon atmosphere. Then they were further processed by casting into copper molds under inert gas atmosphere to form amorphous strips with 1 mm thickness. The measurements were done using a Perkin-Elmer DSC7. The sample sizes range from 4 to 50 mg. All samples were first heated up above the glass transition temperature to 443 K with a rate of 0.33 K/s and cooled with a rate of 3.3 K/s back to ambient temperature to ensure the same thermal history. The calorimeter was recalibrated for every heating rate using the melting transition of indium and zinc standards in order to account for the temperature shift on changing heat rates. A

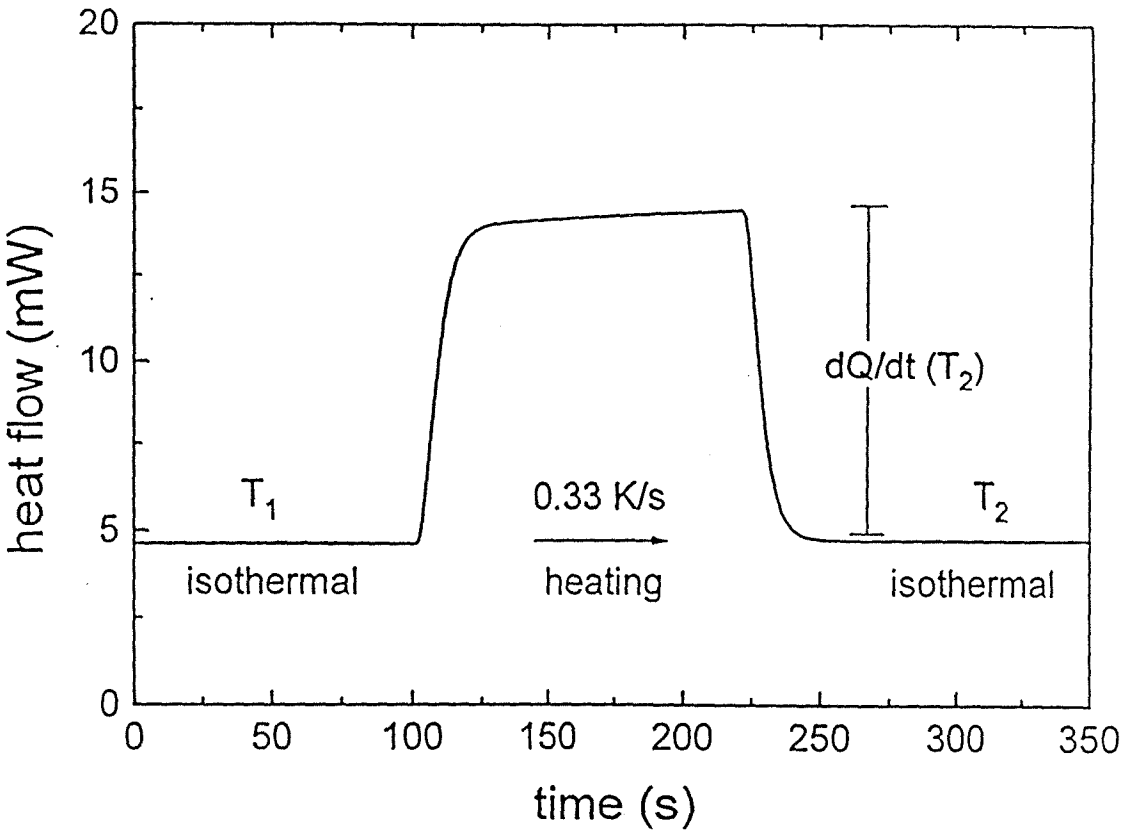

Fig. 3.1 Typical specific heat capacity measurement with a DSC at the temperature T_2. Reproduced from ref. 9.

second run for each specimen was directly carried out after the first cycle without changing the conditions of the measurement to construct a baseline.

The absolute values of the specific heat capacity in the amorphous alloys up to 485 K, the crystallized samples up to 725 K (melting point), and liquid from the melting point to 843 K were determined in reference to a sapphire standard. The principle of the measurement is shown in Fig. 3.1 [9].

The sample is first heated to a certain temperature with a constant rate of 0.33 K/s and then held there isothermally for 180 s. This results in a step of the heat flux dQ/dt:

$$\frac{dQ}{dt} = (\frac{\partial Q}{\partial t})_{\dot{T}\neq 0} - (\frac{\partial Q}{\partial t})_{\dot{T}=0} = C \cdot \frac{dT}{dt} \quad . \tag{3.1}$$

The term $(\frac{\partial Q}{\partial t})_{\dot{T}\neq 0}$ corresponds to the power which is necessary to heat the sample and the pan with an overall heat capacity C and hold it on a certain temperature. $(\frac{\partial Q}{\partial t})_{\dot{T}=0}$ is the power which is supplied to keep the temperature just constant. To determine the specific heat capacity of the sample, the heat capacity of the pan has to be determined. Hence, a second measurement with sapphire and a third with the empty pan were carried out. The specific heat capacity of the sample is then calculated by the following formula:

$$C_p(T)_{sample} = \frac{\dot{Q}_{sample} - \dot{Q}_{pan}}{\dot{Q}_{sapphire} - \dot{Q}_{pan}} \cdot \frac{m_{sapphire} \cdot \mu_{sample}}{m_{sample} \cdot \mu_{sapphire}} \cdot C_p(T)_{sapphire} \tag{3.2}$$

where m_i is the mass, μ_i is the mole mass and $C_p(T)_{sapphire}$ is the specific heat capacity of sapphire. This procedure was done every 10 K. The samples were contained in

molybdenum pans and scanned in a flowing argon atmosphere to reduce oxidation since some samples were heated above melting temperature.

3.2.2 Results

The glass transition, crystallization and the melting behaviors of $Mg_{65}Cu_{25}Y_{10}$ alloy were monitored in DSC scans for various heating rates. Fig. 3.2 shows a typical DSC scan. It starts with an endothermal heat effect due to the glass transition then follows with several exotherms corresponding to several steps of crystallization. The first deep exotherm starting at about 468 K is the transformation of the supercooled liquid to the crystalline phase Mg_2Cu. The sample starts to melt at the eutectic temperature 727 K followed by complete melting at the liquid temperature 739 K. The scan shows a relatively sharp single melting endotherm. This means the composition $Mg_{65}Cu_{25}Y_{10}$ is almost at the ternary Mg-Cu-Y eutectic point.

The onset of the glass transition temperature T_g and the crystallization temperature T_x are strongly dependent on the heating rates. Fig. 3.3 shows the specific heat capacity of the amorphous phase throughout the glass transition into the undercooled liquid with respect to the crystalline phase for different heating rates. The absolute values for C_p of the crystal and amorphous alloy were measured with respect to sapphire standards. One can see that the onset of the glass transition temperature, as well as the temperature on which the samples reach the undercooled liquid region, increases with faster heating rate. In the undercooled liquid region, C_p is a well defined decreasing function with increasing temperature.

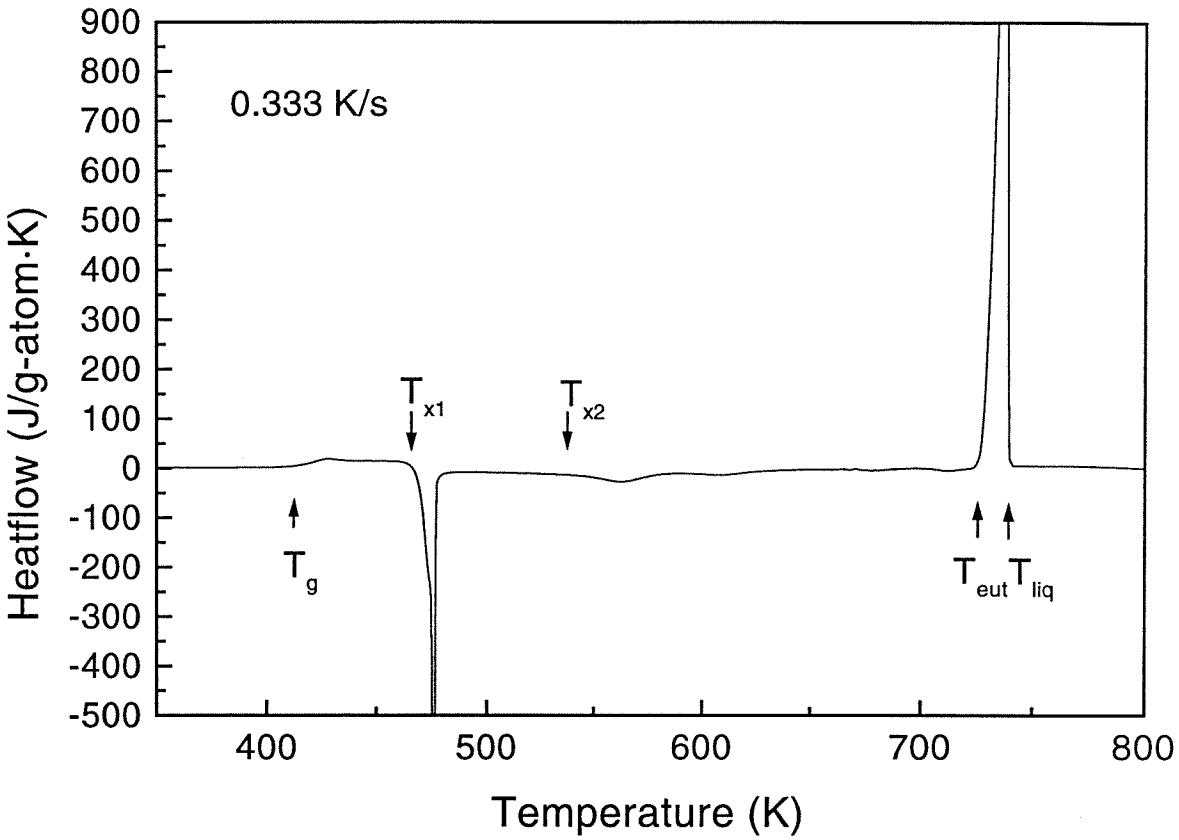

Fig. 3.2 DSC scan of amorphous $Mg_{65}Cu_{25}Y_{10}$ with a heating rate of 0.333 K/s.

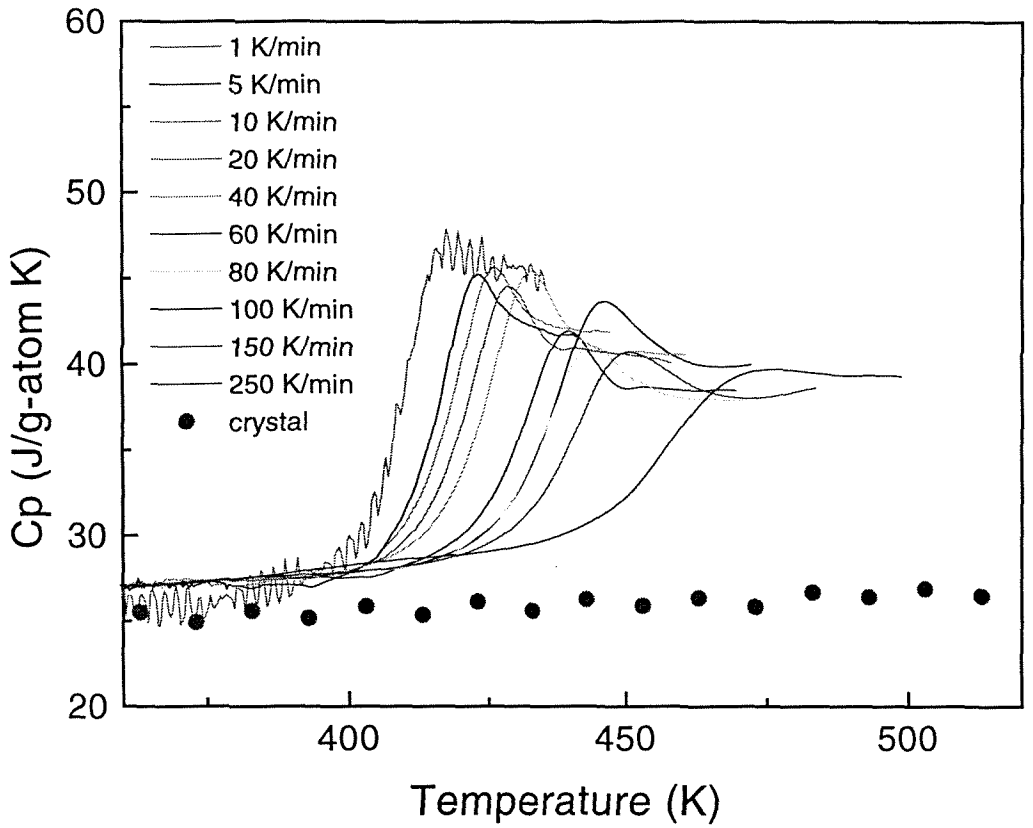

Fig. 3.3 The specific heat capacity from the amorphous phase throughout the glass transition into the undercooled liquid for different heating rates. The specific heat capacity data of the crystallized samples were measured in steps of 10 K in reference to a sapphire standard.

Fig. 3.4 shows measured specific heat capacities of the undercooled liquid, the crystal and the melting liquid. The specific heat capacities around the glass transition region are not presented since they do not represent a thermodynamic equilibrium, or metastable equilibrium state. According to Kubaschewski *et al.* [10], the temperature dependence of the specific heat capacity of the undercooled liquid far above Debye temperature can be expressed mainly as a T^{-2} law as follows:

$$C_p=3R+b\cdot T+c\cdot T^{-2}, \qquad (3.3)$$

where R=8.314 J/g-atom·K. The curve is extrapolated down to the Kauzmann temperature, T_k, which represents the lower bound for the glass transition for thermodynamical reasons. The Kauzmann temperature T_k is the point on which the entropy of the undercooled liquid reaches the entropy of the crystal.

From the measured specific heat capacity data, we can calculate some thermodynamic functions of the $Mg_{65}Cu_{25}Y_{10}$ alloy as a function of temperature. The Gibbs free energy of undercooled liquid with respect to the crystal, $\Delta G_{l\text{-}x}(T)$, can be calculated by integrating the specific heat capacity difference according to equation

$$\Delta G_{l-x}(T) = \Delta H_f - \Delta S_f \cdot T_f - \int_T^{T_f} \Delta C_p^{l-x}(T')dT' + T\int_T^{T_f} \frac{\Delta C_p^{l-x}(T')}{T'}dT' \qquad (3.4)$$

where ΔH_f and ΔS_f are the enthalpy and entropy of fusion, respectively, at the temperature T_f. T_f is the temperature where the Gibbs free energy of the crystal and the liquid are equal. $\Delta C_p^{l\text{-}x}$ is the difference in specific heat capacity between liquid and crystal. Although the T_f is not exactly known for the alloy, from the DSC curve near the melting temperature, we can see the alloy is very close to the eutectic

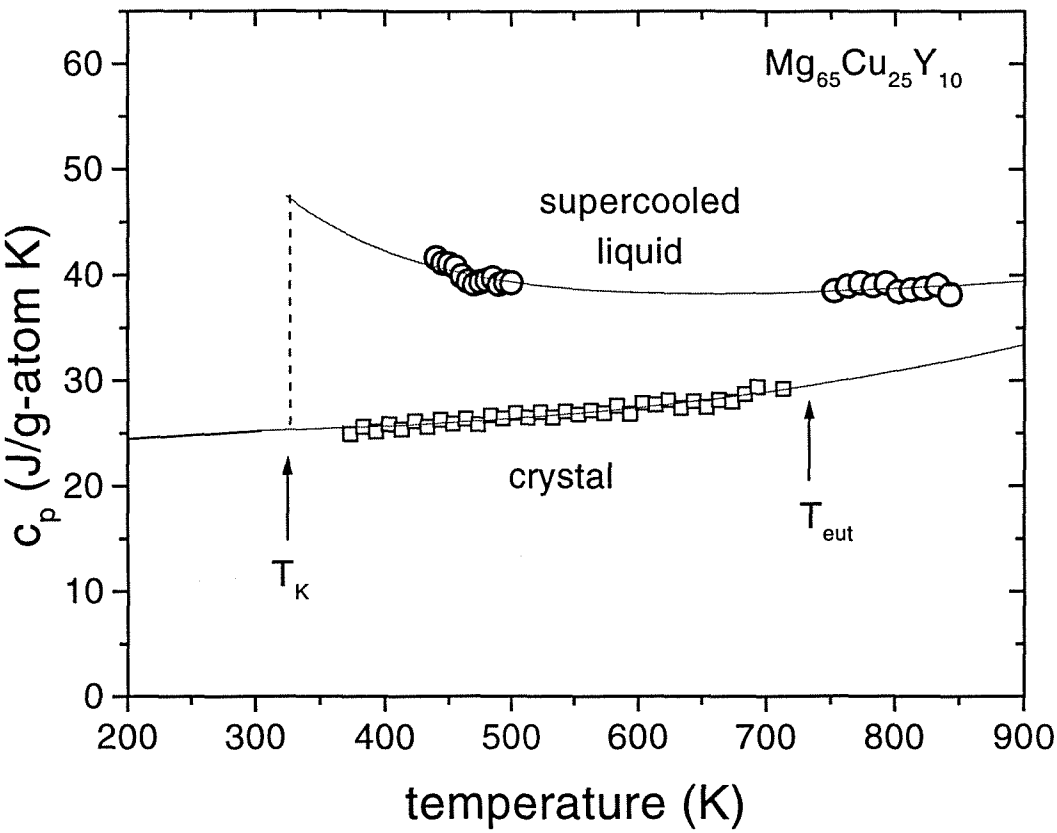

Fig. 3.4 Measured specific heat capacity of the liquid, undercooled liquid and the crystal phase.

composition and the starting and ending points of the melting peak differs only several degrees. T_f is somewhere within the melting peak. Here we choose the eutectic temperature as T_f and the error should be very small.

The calculated entropy of the undercooled $Mg_{65}Cu_{25}Y_{10}$ liquid with respect to crystal is shown in Fig. 3.5. The entropy of the undercooled liquid decreases with increasing undercooling until it reaches the entropy of the crystal at Kauzmann temperature which equals to 320 K. The undercooled liquid below T_k cannot exist according to Kauzmann paradox [11] due to the fact that the liquid should not have an entropy smaller than that of the crystal.

Fig. 3.6 shows the calculated enthalpy difference between undercooled liquid and the crystalline state. The specific heat is integrated from T_f down to the Kauzmann temperature T_k. Since the difference in specific heat capacity between amorphous and crystal phase is very small, the enthalpy function below T_k is virtually constant. However, in real experiments, it is very hard to achieve the states below about 410 K since those states belong to ideal undercooled liquid and glass which require extremely slow cooling rate to form. In practice, the liquid freeze to a glass through the glass transition and with larger cooling rate, more residual enthalpy and entropy are frozen in the glass.

The calculated Gibbs free energy function with respect to the crystalline state is plotted in Fig. 3.7. Since the entropy of fusion for this alloy is relatively small, the slope of the Gibbs free energy curve just below the melting point is small which leads to a small driving force for crystallization. The small driving force turns out to

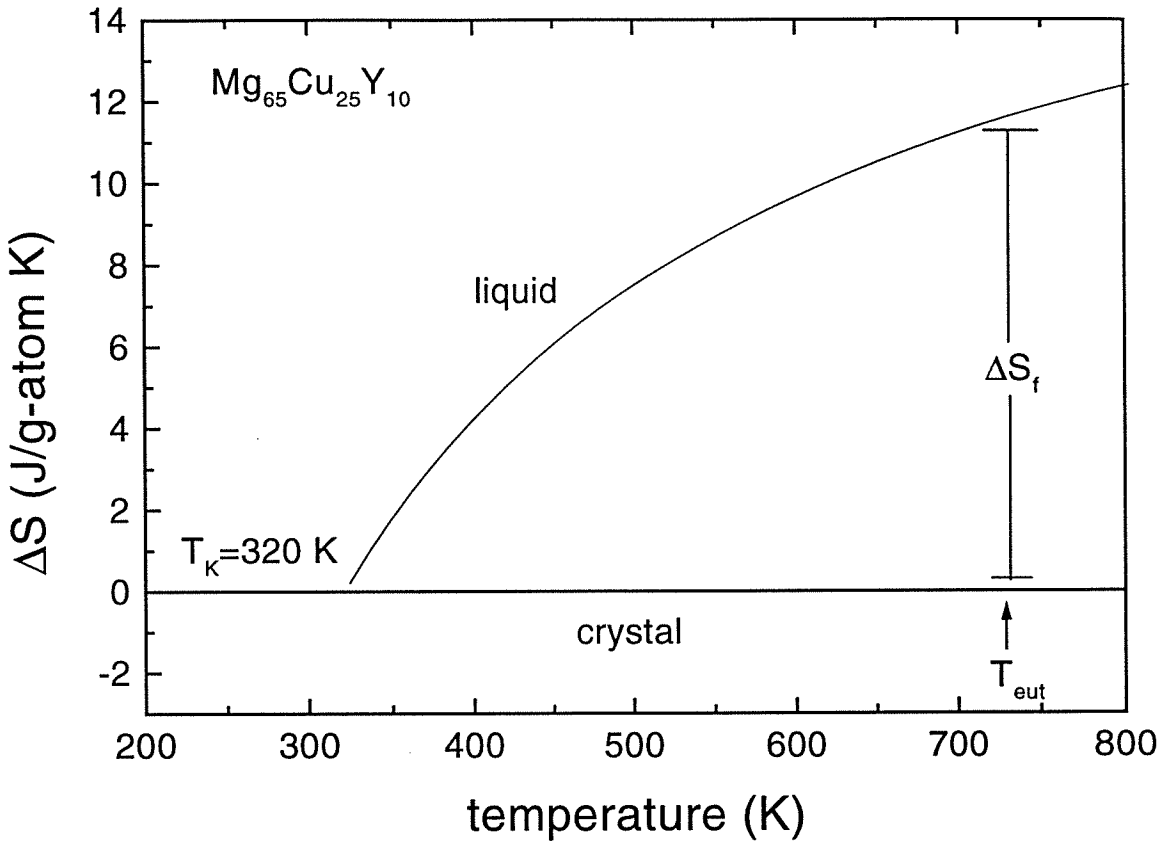

Fig. 3.5 Entropy of the undercooled liquid with respect to the crystal, including the entropy of fusion, ΔS_f, and the Kauzmann temperature, T_k.

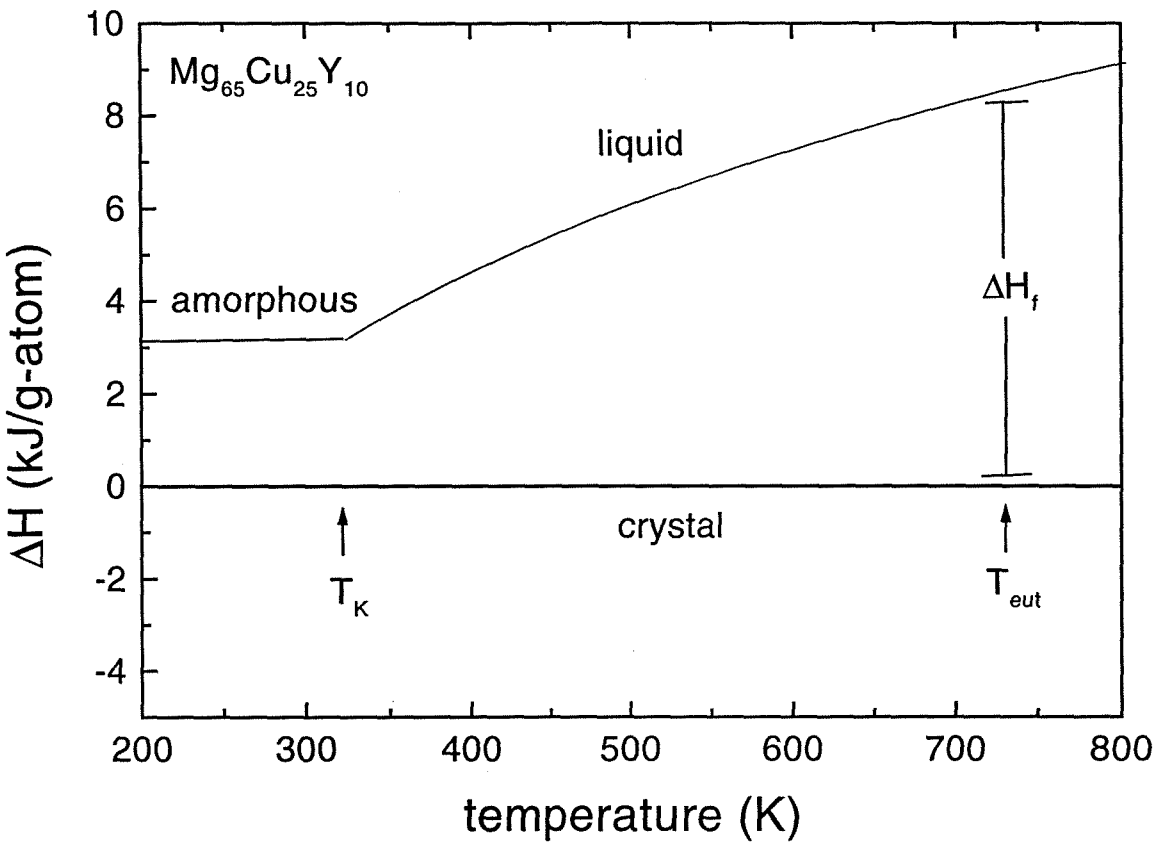

Fig. 3.6 Enthalpy of the undercooled liquid with respect to the crystal as a function of temperature.

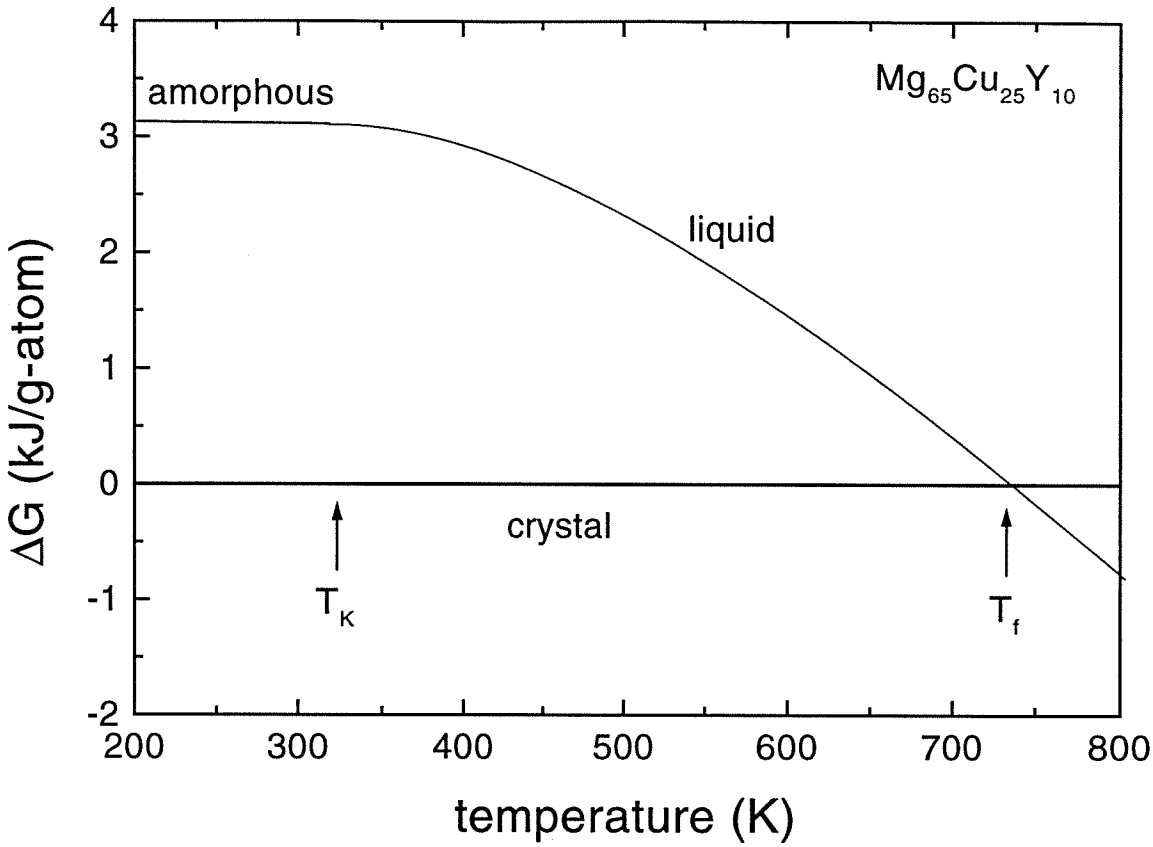

Fig. 3.7 Gibbs free energy of the undercooled liquid with respect to the crystal as a function of temperature.

be one crucial point in understanding the high glass forming ability in bulk metallic glass formers. In Fig. 3.8, the Gibbs free energy differences between the undercooled liquid and the crystalline mixture is plotted for a selection of eutectic glass forming systems. The glass former with the lower critical cooling rates, R_c, have smaller Gibbs free energy differences than the glass formers with high critical cooling rates. The driving force for crystallization decreases with increasing bulk metallic glass forming ability. This originates mainly from the smaller entropy of fusion since the entropy of fusion determines the slope of the free energy curve at melting point. The small entropy of these deep eutectic bulk metallic glass forming systems at melting point suggests that they have a small free volume and a tendency to develop short range order or phase separation which will be investigated in Chapter 5 on a MgCuYLi alloy.

3.3 Kinetics

3.3.1 Experimental methods

The method we used to measure viscosity is flexure or three point beam-bending. The schematic diagram is shown in Fig. 3.9. A load is applied to the center of a beam of uniform cross-section supported on both ends. By measuring the deflection of the center of the beam with time, the viscosity can be derived. Viscosity in the range from 10^8 to 10^{15} poise can be measured by this method. The three-point beam-bending has been used to measure the viscosity of silicate glasses [11].

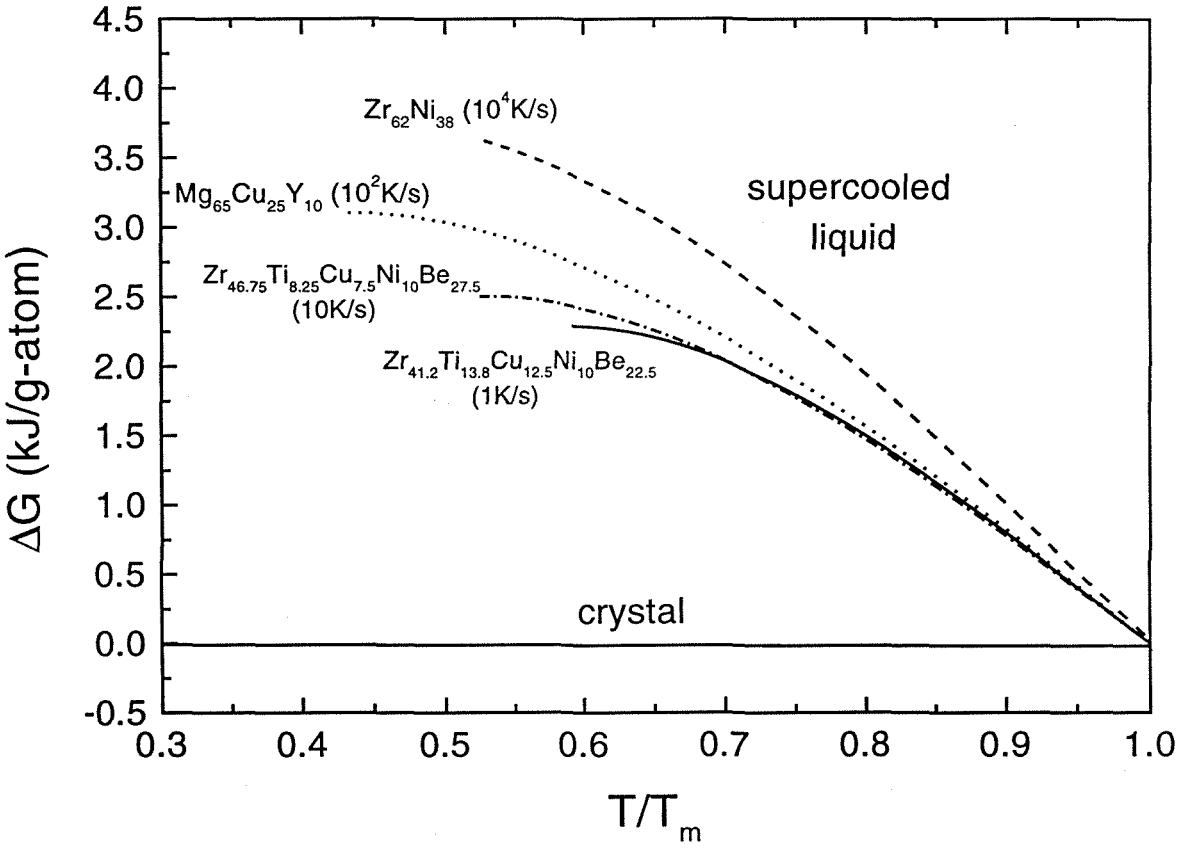

Fig. 3.8 Gibbs free energy difference between the undercooled liquid and the crystalline mixture for different glass forming alloys.

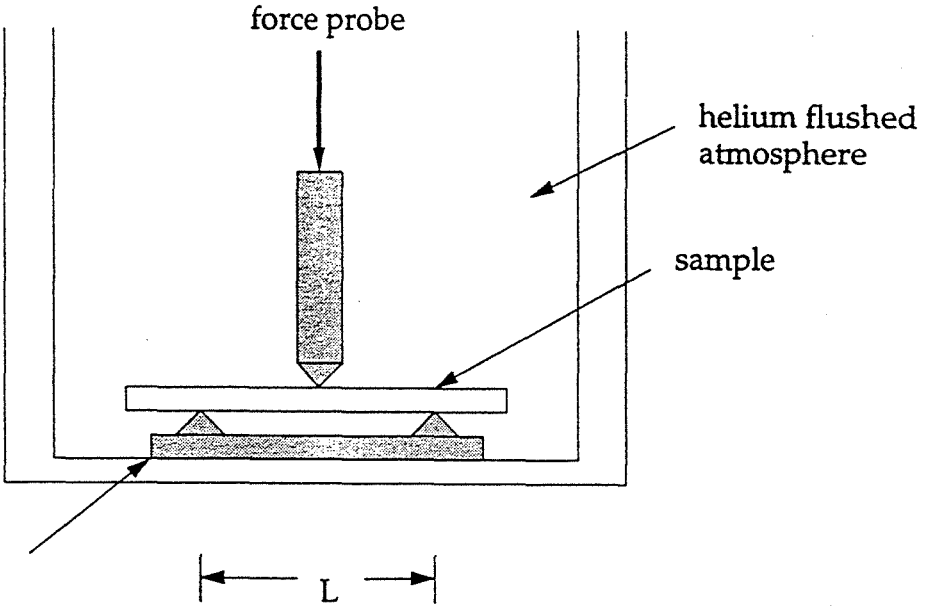

Fig. 3.9 Schematic diagram for three point beam-bending or flexure.

The viscosity in Pa·s can be found using the equation [12, 13, 14]:

$$\eta = \frac{gL^3}{144 I_c \nu}\left(M + \frac{5\rho AL}{8}\right) \tag{3.5}$$

where g is the gravitational constant (9.8 m/s^2), I_c the cross-section moment of inertia (m^4), ν the midpoint deflection rate (m/s), M the applied load (kg), ρ the density of the glass (kg/m^3), A the cross-sectional area (m^2), and L the support span (for out apparatus, $L=5.08\times10^{-3}$ m).

The experimental apparatus used was a Perkin-Elmer Thermal Mechanical Analyzer (TMA 7). Beam samples of $Mg_{65}Cu_{25}Y_{10}$ with different rectangular cross-sections were cut from 1 mm thick amorphous strips from mold-casting. Typical length of the beams is 8 mm and typical cross-section is 1×0.5 mm^2. The force applied varies from 20 mN to 1000 mN depending on the measured temperature. Samples were heated from room temperature to the measured temperature with a heating rate of 0.833 K/s then isothermally annealed at that temperature for different times ranging from 30 min to 5000 min.

3.3.2 Results

Fig. 3.10 shows the viscosity of $Mg_{65}Cu_{25}Y_{10}$ in an Ahhrenius plot obtained from three-point beam-bending method. The data were fitted by a Vogel-Fulcher-Tammann (VFT) equation

$$\eta = \eta_0 \cdot \exp\left(\frac{D \cdot T_0}{T - T_0}\right) \tag{3.6}$$

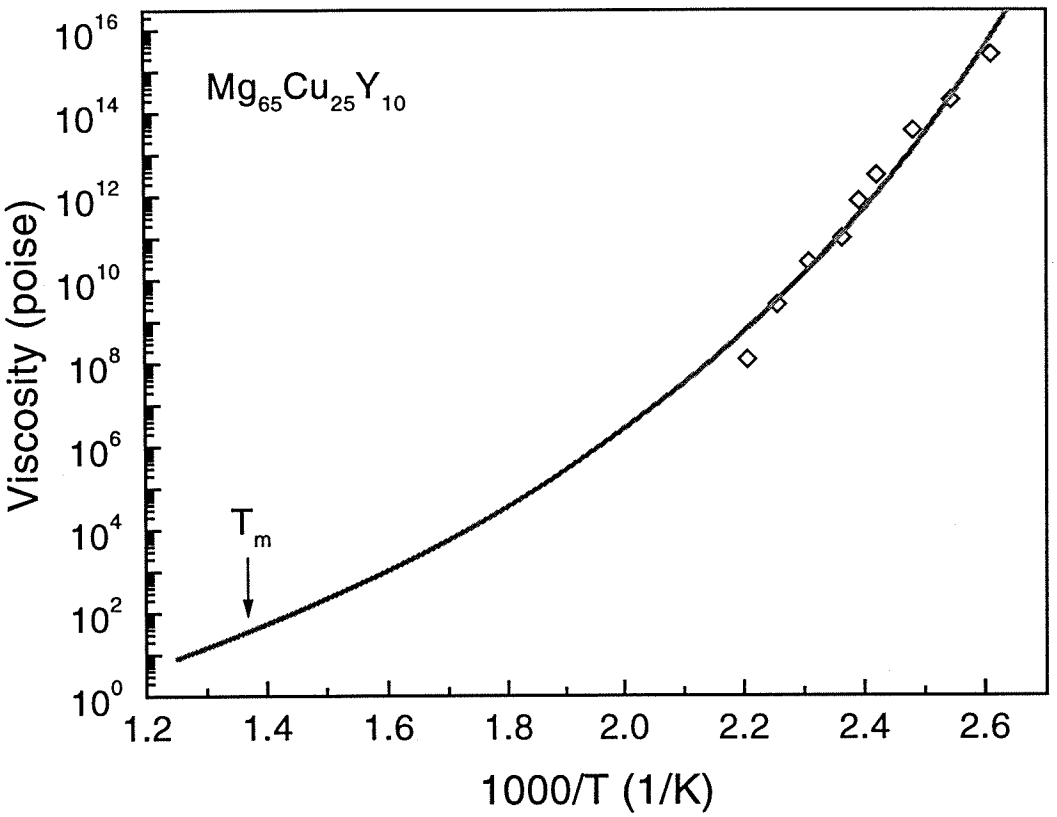

Fig. 3.10 Viscosity of the amorphous and supercooled liquid for $Mg_{65}Cu_{25}Y_{10}$.

in a modification that was proposed by Angell [15]. In this formulation D is the fragility parameter and T_0 is the VFT temperature. The best fit of the experimental data yields D=21.1 and T_0=260 K. The value η_0 was set as 3×10^{-4} poise according to the relation $\eta_0=N_A \cdot h/V$, where, N_A is Avogadro's constant, h is Planck constant and V is the molar volume [16].

The temperature corresponding to viscosity 10^{13} Poise is 404 K, which is consistent with the onset value (T_g=401 K) of the calorimetric glass transition for a heating rate of 1 K/min.

3.3.3 Strong glass behavior

Since different glasses have different values of T_g, in order to compare the various glasses, an interpretation was developed by Angell [15] by plotting the log of the viscosity as a function of T_g/T, an Arrhenius plot with inverse temperature reduced by the glass transition temperature. Fig. 3.11 shows the comparison of viscosities of a selection of some metallic and non-metallic glasses. The silicate and the polymer glass (o-terphenyl) exhibit the two extremes in viscous behavior with temperature, called strong and fragile liquid behavior, respectively. In the Vogel-Fulcher-Tammann equation, Arrhenius behavior is the limit where $D\rightarrow\infty$ or $T_0\rightarrow0$. The fragility parameter, D, determines how closely the system's viscosity approaches the Arrhenius law. For strong glasses like silicates, a small T_0 is found and D is of order 100. For fragile glasses like polymers, a T_0 is close to T_g and D can be as low

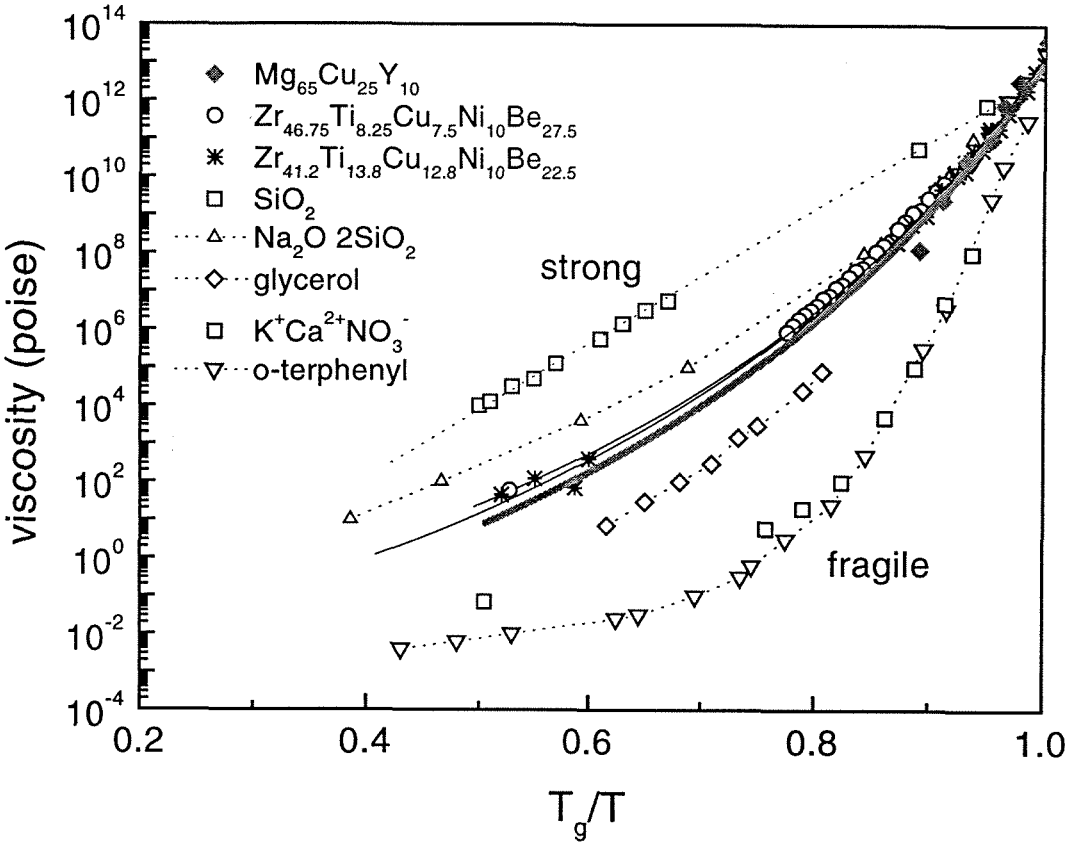

Fig. 3.11 Angell plot of the viscosities of some bulk metallic glasses and several non metallic "strong" and "fragile" glasses.

as 2 [17]. Metallic glasses are between these two extremes. The temperature dependence of the viscosity of $Mg_{65}Cu_{25}Y_{10}$ alloy is found to behave similar to the relatively strong sodium silicate glasses, also very close to the good glass former Zr-Ti-Cu-Ni-Be system [18].

The strong liquid behavior plays an important role in understanding the superior glass forming ability compared to other metallic liquids. Fig. 3.12 shows the comparison of viscosity of some glasses. Fragility parameters and the critical cooling rates are indicated in the plot. One observes the general trend that critical cooling rates decrease with increasing fragility parameters. That means the stronger the glass, the lower the critical cooling rate and the higher the glass forming ability. The reason is that the viscosity is a contributing factor to the nucleation rate of crystals. According to eq. 1.6, the nucleation rate is proportional to $1/\eta(T)$. High viscosity in the undercooled melt decrease the nucleation rate and thus enhance the glass forming ability compared to undercooled liquids that exhibit low viscosity. As seen in Fig. 3.12, $1/\eta(T)$ is several orders of magnitude higher for strong glasses in the region below the melting point to T_g compared to most fragile liquids. On the other hand, when heating a strong glass into the supercooled liquid region, the viscosity decreases much slower than that in the fragile liquid and the kinetics for crystallization stays sluggish. This contributes to the high thermal stability of the supercooled liquid in bulk metallic glass forming systems in the glass transition region and allows extensively studies for metallic systems at and above T_g.

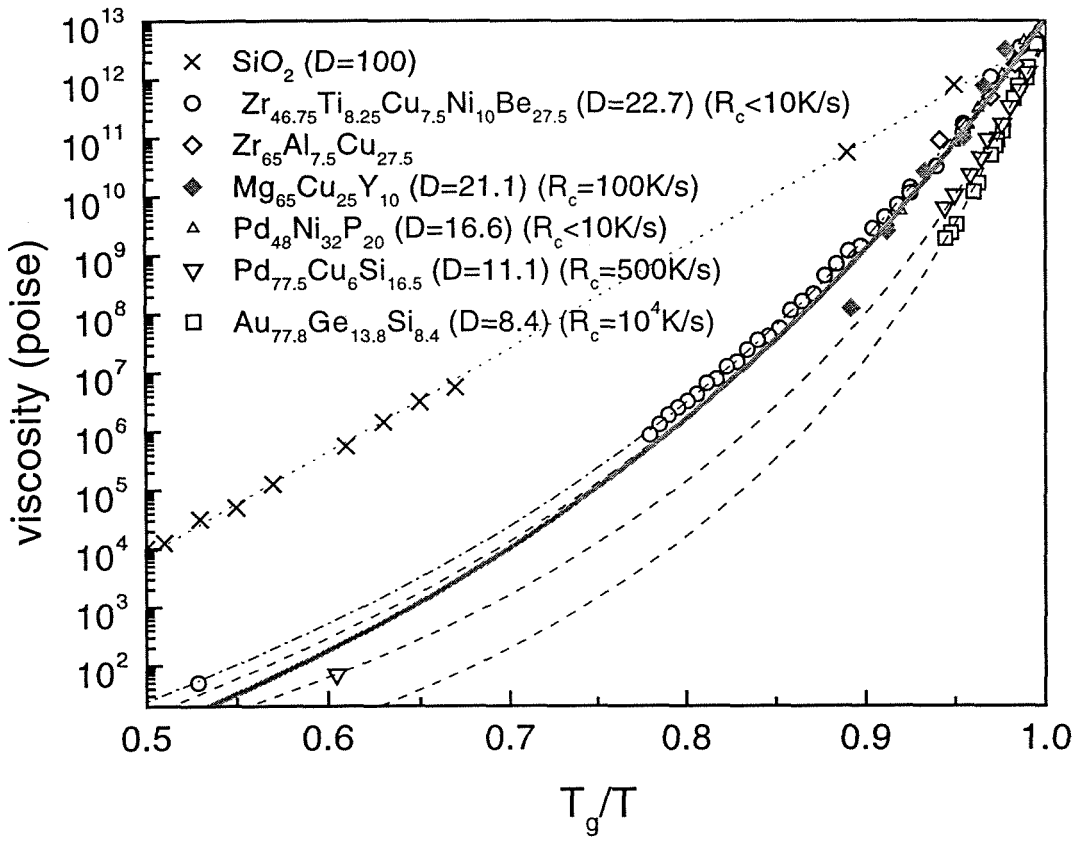

Fig. 3.12 Angell plot of the viscosities of several glasses. Fragility parameters and the critical cooling rates are indicated.

3.4 Conclusion

The thermodynamics and kinetics of $Mg_{65}Cu_{25}Y_{10}$ alloy were studied. Absolute values of C_p were measured with respect to sapphire standards for amorphous, crystal, superercooled liquid, and melt. C_p for the liquid is a decreasing function of temperature and can be expressed mainly as a T^{-2} law. From the absolute C_p data of liquid and crystal, the entropy, enthalpy, and Gibbs free energy as a function of temperature were calculated. The calculations show that the Gibbs free energy difference between liquid and solid state stays relatively small for undercoolings. The relatively small Gibbs free energy difference appears to be a contributing factor in the high glass forming ability of the alloy. The Kauzmann temperature is calculated to be 320 K, representing the lower bound for the kinetically observed glass transition. The viscosities of the amorphous through glass transition temperature into the supercooled liquid region were measured using three-point beam-bending method. The viscosity ranges from 10^8 to 10^{15} poise. The viscosity above the glass transition region exhibits a Vogel-Fulcher behavior with a small T_0 compare to glass transition temperature. From the fragility parameter, $Mg_{65}Cu_{25}Y_{10}$ is a relatively strong glass and similar to good glass former $Zr_{46.75}Ti_{8.25}Cu_{7.5}Ni_{10}Be_{27.5}$. Both the small driving force for nucleation and the sluggish kinetics in the supercooled liquid retard the nucleation of crystals from a homogeneous liquid substantially. As will be shown in Chapter 5, the pathway

towards crystalline state in bulk metallic glasses proceeds via phase separation in the liquid state with subsequent local primary crystallization.

REFERENCES

[1] A. Inoue, T. Zhang, and T. Masumoto, Mater. Trans., JIM, **31**, 425 (1991).

[2] T. Zhang, A. Inoue, and T. Masumoto, Mater. Trans., JIM, **32**, 1005 (1991).

[3] A. Inoue, A. Kato, T. Zhang, S. G. Kim, and T. Masumoto, Mater. Trans., JIM, **32**, 609 (1991).

[4] A. Peker and W. L. Johnson, Appl. Phys. Lett., **63**, 2342 (1993).

[5] R. Busch, Y. J. Kim, and W. L. Johnson, J. Appl. Phys., **77**(8), 4039 (1995).

[6] E. Bakke, R. Busch, and W. L. Johnson, Appl. Phys. Lett., **67**(22), 3260 (1995).

[7] U. Geyer, S. Schneider, W. L. Johnson, Y. Qiu, T. A. Tombrello, and M. P. Macht, Phys. Rev. Lett., **75**, 2364 (1995).

[8] R. Busch, Y. J. Kim, W. L. Johnson, A. J. Rulison, W. K. Rhim, and D. Isheim, Appl. Phys. Lett., **66**, 3111 (1995).

[9] R. Busch, Y. J. Kim, and W. L. Johnson, 7th Int. Symp. On Experimental Methods for Microgracity Mat. Sci., TMS Meeting, Vegas, Feb. 13-15, 1995.

[10] O. Kubaschewski, C. B. Alcock, and P. J. Spencer, *Materials Thermochemistry*, 6th ed. (Pergamon, New York, 1993).

[11] W. Kauzmann, Chem. Rev., **43**, 219 (1948).

[12] H. E. Hagy, Jour. Am. Ceram. Soc., **46**, 93 (1963).

[13] F. T. Trouton, Proc. Roy. Soc. (London) **77**, 426 (1906).

[14] M. Reiner, *Rheology*, Vol. **1** (ed F. R. Eirich), Academic Press, New York, 9 (1956).

[15] C. A. Angell, Science, **267**, 1924 (1995).

[16] S. V. Nemilov, Glass Physics and Chemistry, **21**, 91 (1995).

[17] D. J. Plazek and K. L. Ngai, Macromolecules, **24**, 1222 (1991).

[18] R. Busch, A. Masuhr, E. Bakke, and W. L. Johnson, Materials Research Society Symposium Proceedings, 455 (1996).

Chapter 4

Phase separation and crystallization of glasses

4.1 Phase separation

Liquid immiscibility is a phenomenon found in binary or multicomponent systems such that over a certain region of temperature and composition, called a miscibility gap, the system exists in equilibrium or metastable equilibrium as two liquid phases of different composition. The process whereby the homogeneous liquid separates into two liquids as it is brought into the two-liquid region is known as phase separation.

Thermodynamically, a liquids exhibits a miscibility gap when the sum of the Gibbs free energies of the two separated phases is less than the Gibbs free energy of a homogeneous solution of the components. The general properties of the miscibility gaps are demonstrated by the phase diagram and the series of Gibbs free energy curves shown in Fig. 4.1 [1]. Consider a binary system, AB, which can exist in the liquid phase either as a single phase or as a two-phase mixture, depending on the temperature. The difference of the Gibbs free energy between the homogeneous solution and two-phase mixture, ΔG, is given by:

$$\Delta G=G_{homo}-G_{mix}=\Delta H-T\Delta S\ . \qquad (4.1)$$

Since in the enthalpy H=U+PV, for condensed phases, PV is small at ordinary pressures and generally the volume difference is small for different phases, hence ΔH is mainly the difference of the internal energy ΔU. Using the nearest-neighbor approximation, i.e., assume that only nearest-neighbor interactions need to be counted for the internal energy, the enthalpy difference is related to composition C as:

$$\Delta H=\alpha C_A C_B , \tag{4.2}$$

Where $C_A+C_B=1$ and α is a constant related to the materials.

The entropy term can be regarded as arising from the entropy of mixing:

$$\Delta S=-R(C_A \ln C_A+C_B \ln C_B) , \tag{4.3}$$

so, we get

$$\Delta G= \alpha C_A C_B+RT(C_A \ln C_A+C_B \ln C_B) . \tag{4.4}$$

If, H for the single homogeneous phase is greater than for a mixture of the components ($\alpha>0$), below a critical temperature $T_c=\alpha/2R$, which in Fig. 4.1 equals to T_2, the free energy curve will exhibit minima at two compositions. Between these two minima, the free energy of the phase-separated mixture is lower than that of the single homogeneous phase and phase separation will take place. The curve of those minima on the phase diagram, shown in Fig. 4.1(f), marks the miscibility gap.

The points on the Gibbs free energy curve at which the second derivative, $\partial^2 G/\partial C^2$, is equal to zero are known as the spinodal points. The locus on the phase diagram of the compositions corresponding to these points forms the spinodal curve,

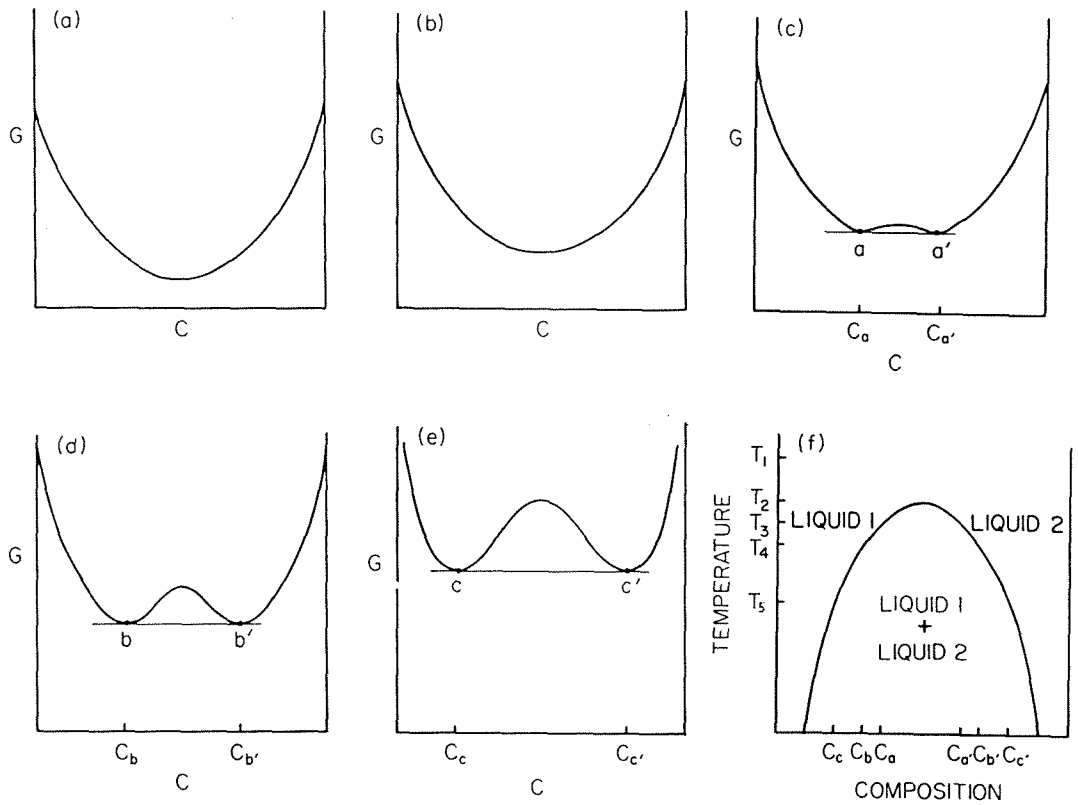

Fig. 4.1 Two-liquid immiscibility. (a-e) show a sequence of Gibbs free energy curves corresponding to the phase diagram shown in (f). (a)$T=T_1$; (b)$T=T_2$; (c)$T=T_3$; (d) $T=T_4$; (e)$T=T_5$. Reproduced from ref. 1.

as shown schematically in Fig. 4.2. The spinodal curve divides the miscibility gap into a metastable and an unstable region [2, 3]. Below the spinodal curve, it is unstable with respect to infinitesimal composition fluctuation and spontaneously separates into two related phases differing only in composition. This process occurs spontaneously without the need for nucleation. In the region between the spinodal and miscibility gap, the single phase liquid is metastable to infinitesimal composition fluctuations and the separation requires a finite fluctuation or nucleus to render the single phase unstable. Fig. 4.3 illustrates schematically the transformation of the phase separation. Above the spinodal, the large compositional difference necessary for stable growth of the new phase ensures that there will be a discrete boundary between the phases, i.e., discrete nuclei will form, even in the early stages of decomposition. While below the spinodal, even regions of very small compositional difference from the matrix can grow stably provided they are large enough in extent. Thus, in the early decompositional stages, the boundary regions between the phases will no longer be sharp and there will simply be a gradual and periodic composition variation throughout the parent solution with quite diffuse boundaries between the high and low composition regions. In the later stages of the transformation, the appearance of the spinodal decomposition product will approach that characteristic of discrete particles and the two modes of transformation will then hardly be distinguishable. Fig. 4.4 shows a computed two-phase structure characteristic of spinodal decomposition, where Λ is the characteristic wavelength.

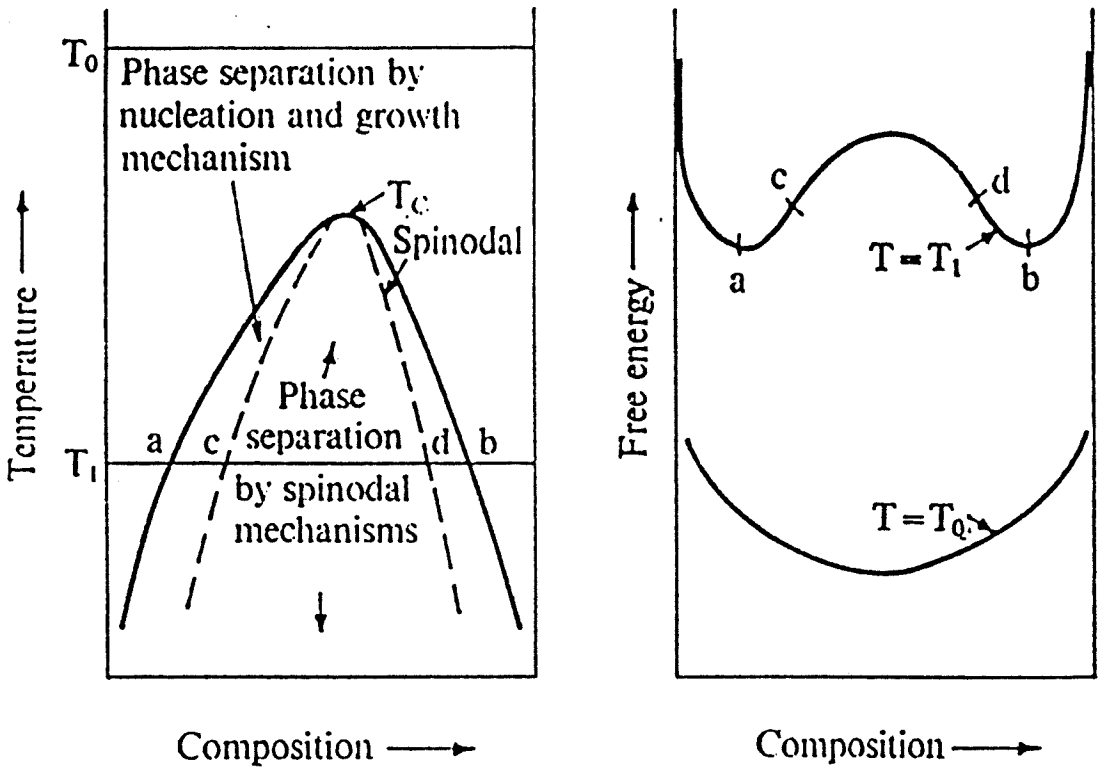

Fig. 4.2 (a)Schematic phase diagram showing the phase boundary and spinodal of a two-liquid immiscibility region. (b)Free energy composition diagrams for the temperatures given in (a). Reproduced from ref. 2.

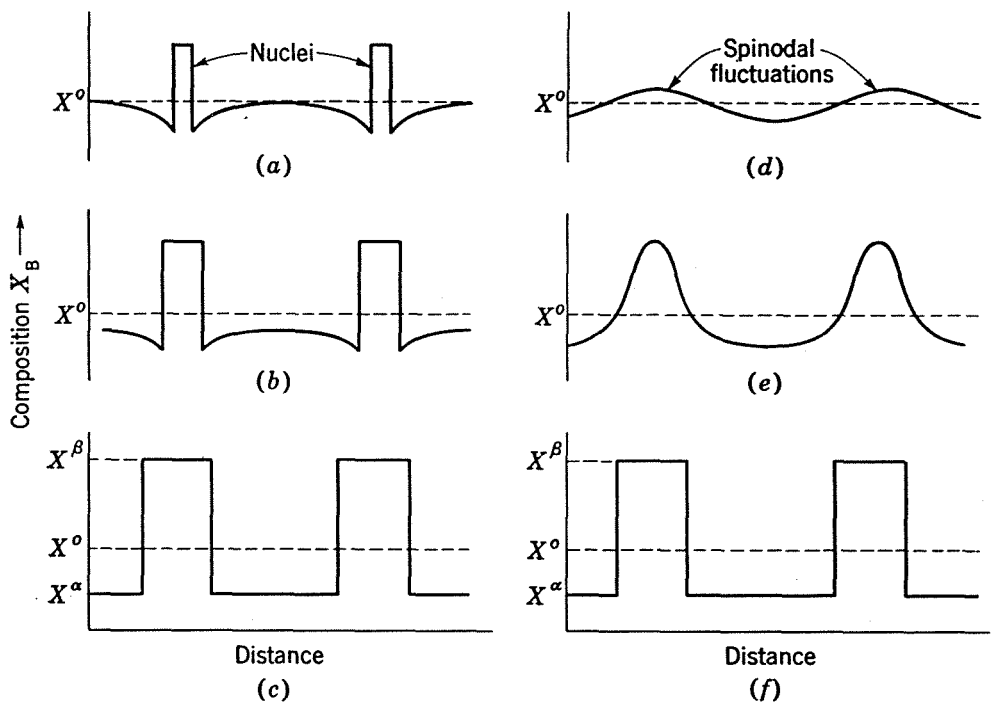

Fig. 4.3 Schematic composition profiles during successive stages of phase separation by (a to c) nucleation and growth and by (d to f) spinodal decomposition. Reproduced from ref. 3.

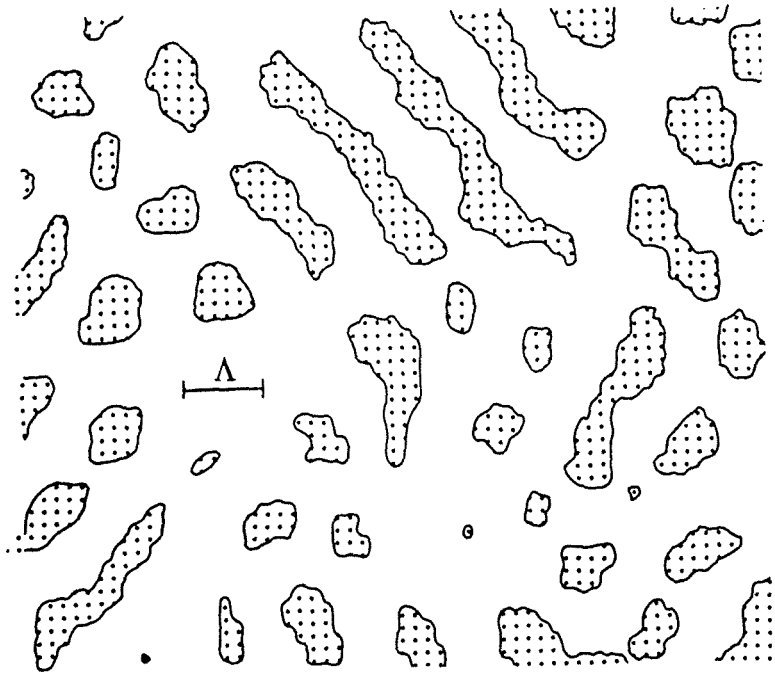

Fig. 4.4 Computed two-phase structure characteristic of spinodal decomposition. Reproduced from ref. 2.

4.2 Phase separation in glasses

Phase separation has been studied in oxide glass systems many years ago [2, 4, 5, 6]. In recent years, decomposition in the amorphous or supercooled liquid state has been reported in many metallic glass forming systems, for example, Ti-Zr-Be [7, 8], Zr-Cu [9, 10], Zr-Co [11] and more recently in several bulk metallic glass forming systems like La-Al-Ni [12] and Zr-Ti-Cu-Ni-Be [13, 14]. The phase separation phenomena has been studied for different metallic glasses using a variety of techniques such as transmission electron microscopy, differential scanning calorimetry, small angle scattering, mossbauer spectroscopy, atom probe field ion microscopy etc. It is found that, in these bulk metallic glass forming systems, the crystallization behavior and glass forming ability are strongly affected by the phase separation phenomena. Phase separation was also found in the Mg-Cu-Y-Li system [15]. From the high resolution transmission electron micrograph shown in Fig. 2.8 (Chapter 2), one can clearly see the evidence of phase separation in the Mg-Cu-Y-Li alloy.

REFERENCES

[1] A. M. Alper (ed.), *Phase Diagrams: Materials Science and Technology*, Vol **1**, (Academic Press, New York, 1970), p313-322.

[2] J. W. Cahn and R. J. Charles, Physics and Chemistry of Glasses, **6**, 181 (1965).

[3] P. Gordon, *Principles of Phase Diagrams in Materials Systems*, (McGraw-Hill, 1968), p46-98.

[4] J. Zarzycki and F. Naudin, J. Non-Cryst. Sol., **1**, 215 (1969).

[5] W. Vogel and K. Gerth, Symposium on nucleation and crystallization in glasses and melts, American Ceramic Society, Columbus, Ohio, p21, (1962).

[6] G. E. Rindone, J. Amer. Ceram. Soc., **45**(1), 7 (1962).

[7] L.E. Tanner and R. Ray, Scripta Metall., **14**, 657 (1980).

[8] A. R. Pelton and L. E. Tanner, in Proceedings of the 5th Intl. Conf. On Rapidly Quenched Metals, edited by S. Steeb and Warlimont, (North Holland, Amsterdam 1985), p747.

[9] D. Deng and A. S. Argon, Acta Metall., **10**, 2011 (1986).

[10] R. Bormann, F. Gärtner, and F. Haider, Mater. Sci. Eng., **97**, 79 (1988).

[11] R. Busch, F. Gärtner, S. Schneider, R. Bormann, and P. Haasen, Mat. Res. Soc. Symp. Proc., **343**, 229 (1994).

[12] A. H. Okumura, A. Inoue, and T. Masumoto, Acta Metall. Mater., **41**, 915 (1993).

[13] R. Busch, S. Schneider, A. Peker, and W. L. Johnson, Appl. Phys. Lett., **67**, 1544 (1995).

[14] S. Schneider, P. Thiyajan, and W. L. Johnson, Appl. Phys. Lett., **68**, 483 (1996).

[15] W. Liu and W. L. Johnson, J. Mater. Res., **11**(9), 2388 (1996).

Chapter 5

Experimental studies of the phase separation and crystallization in the $Mg_{62}Cu_{25}Y_{10}Li_3$ alloy

5.1 Experiment

$Mg_{62}Cu_{25}Y_{10}Li_3$ alloys were prepared by induction melting a mixture of the elements of purity ranging from 99.9% to 99.999% on a water-cooled silver boat under a Ti-gettered argon atmosphere. The ingots were repeatedly turned over and remelted to ensure homogeneity. Small pieces of samples, typically 90 mg, were levitation-melted in a high frequency coil and quenched into thin foils in a twin-piston Bühler splat quencher with a cooling rate of about 10^6 K/s [1]. The splat quencher chamber was first pumped to vacuum of about 10^{-3} Pa and then filled with pure argon in order to keep the samples clean. The average thickness of the thin foils from quenching is about 50 μm. To get bulk samples, ingots of about 1-2 g were further remelted under vacuum in a quartz tube using a rf induction coil and then injected in a copper mold under argon at about 1 atm pressure to form 1 mm thick strips. The cooling rate of the casting process is about 10^3 K/s.

Wide angle x-ray diffraction was done by a Phillips diffractometer using Cu-K_α radiation. For the DSC experiments, a Perkin-Elmer DSC 7 calorimeter was used. Microstructural characterization was performed by a Philips TEM430 operating at

300 KV. To prepare TEM specimens, small pieces of samples were embedded in epoxy and cut to approximately 50-80 nm thick sections by thin sectioning microtomy. For small angle x-ray scattering (SAXS) investigations, disks with diameter of 3 mm were cut from splat-quenched samples. These disks were annealed near the glass transition temperature at 135 °C for different times. The SAXS measurements were carried out at SAXS beamline 4-2 at the Stanford Synchrotron Radiation Laboratory [2]. The small angle neutron scattering (SANS) measurements were carried out at the Intense Pulsed Neutron Source at Argonne National Laboratory and the casting strip samples were used.

5.2 Results and discussion

Fig. 5.1 shows a comparison of DSC scans with a heating rate of 40 K/min for $Mg_{62}Cu_{25}Y_{10}Li_3$ in the as-prepared state and the states annealed at 135 °C for 60 and 120 min. For the as-prepared sample, the primary crystallization begins at 177 °C corresponding to the nanoscale bcc-Mg_7Li_3 phase. The second exothermic peak near 200 °C is due to the crystallization of the remaining amorphous matrix to the intermetallic Mg_2Cu phase [3]. Distinct changes are observed for the scans of annealed samples. The width of the undercooled liquid region decreases, the primary crystallization signal broadens and its magnitude decreases with annealing time. Also one notices that the crystallization temperature for the Mg_2Cu phase decreases.

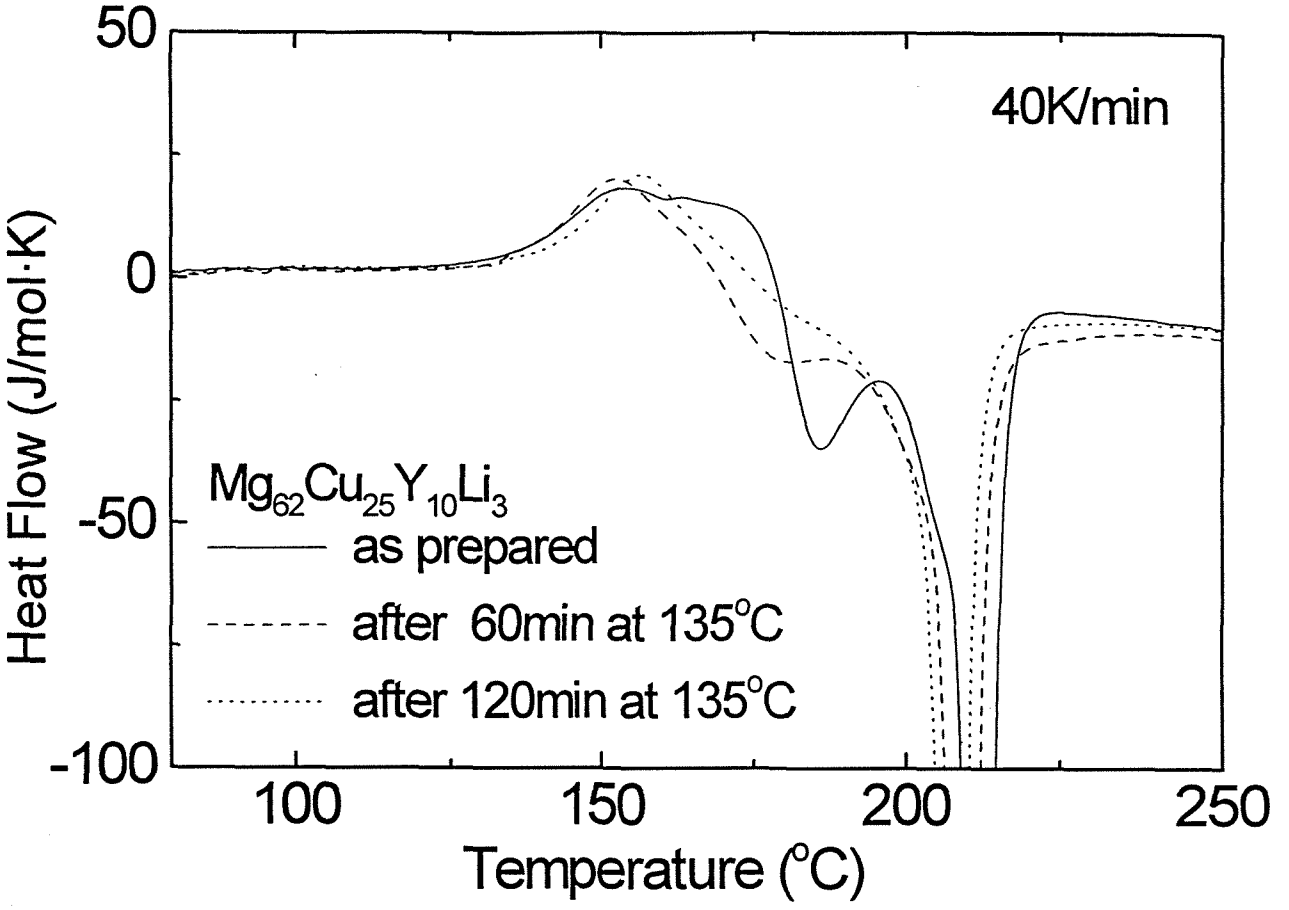

Fig. 5.1 DSC scans for $Mg_{62}Cu_{25}Y_{10}Li_3$ samples heat treated for different times at 135 °C with a heating rate of 40 K/min.

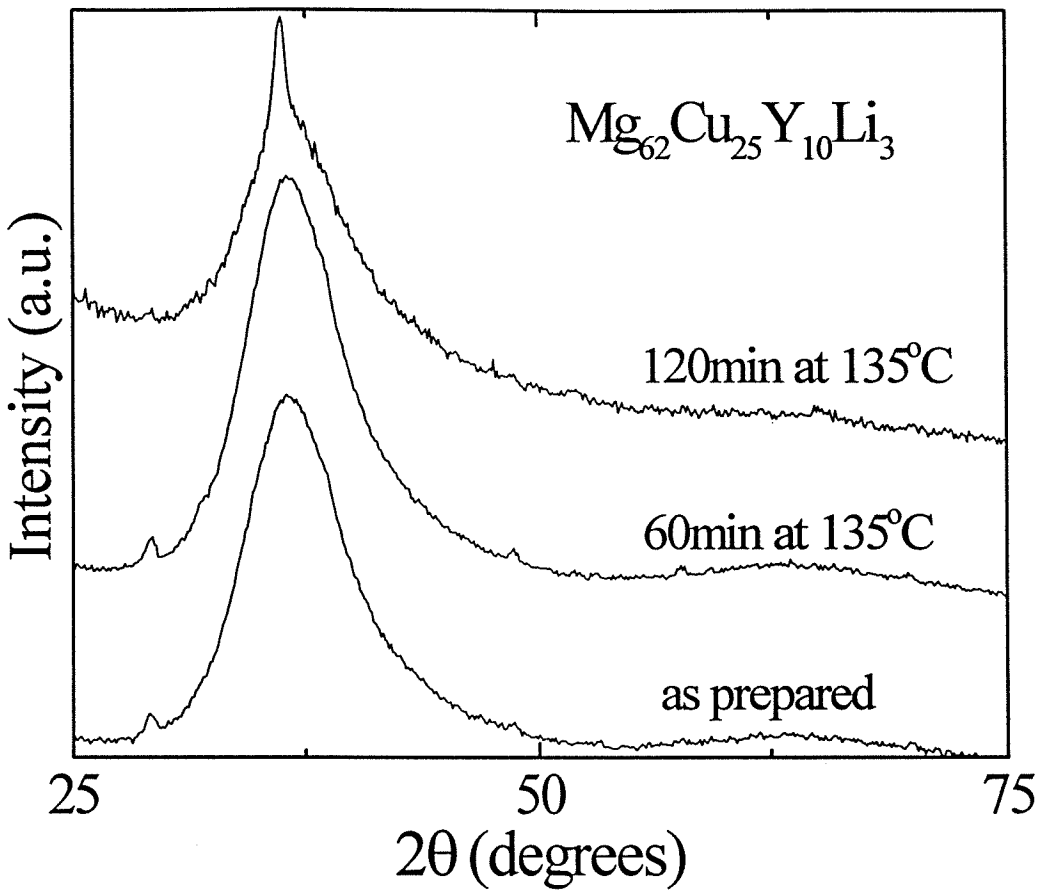

Fig. 5.2 X-ray diffraction patterns of the splat-quenched $Mg_{62}Cu_{25}Y_{10}Li_3$ in the as-prepared state and in samples annealed at 135 °C for 60 and 120 min, respectively.

The wide angle x-ray diffraction patterns of splat-quenched $Mg_{62}Cu_{25}Y_{10}Li_3$ sample in the as-prepared state and in samples annealed at 135 °C for 60 and 120 min are shown in Fig. 5.2. These data indicate that all samples are in general amorphous. The sample annealed for 120 min shows crystalline contribution to the diffraction pattern. The corresponding phase is bcc-Mg_7Li_3. Previous TEM studies of as prepared bulk samples showed small nanocrystals of size about 20-60 Å embedded in an amorphous matrix, but x-ray diffraction could not detect the crystalline phase [3].

Fig. 5.3 shows bright-field, dark-field, and selected area diffraction patterns TEM images of splat-quenched $Mg_{62}Cu_{25}Y_{10}Li_3$ sample annealed at 135 °C for 60 min. The inside "fat" ring in the diffraction pattern looks like one single ring at the first glance. But if observed closely, one can see that it actually contains double rings which are very close to each other. The dark-field image taken from the most inner ring showed almost no crystals which means this ring corresponds to the amorphous. The dark-field image shown in Fig. 5.3 was taken from the outer ring which showed some crystal particles with an average size of about 30 Å. There are some lighter regions with size about 250 Å in the bright-field image. These regions are not bigger crystal particles, instead, they contain much less crystals from the dark-field image. In the bright-field image, one can see some microtoming knife marks cross the brighter regions. Usually there is thickness difference across the knife marks. Since the brightness of the regions does not change on different sides of the marks, the

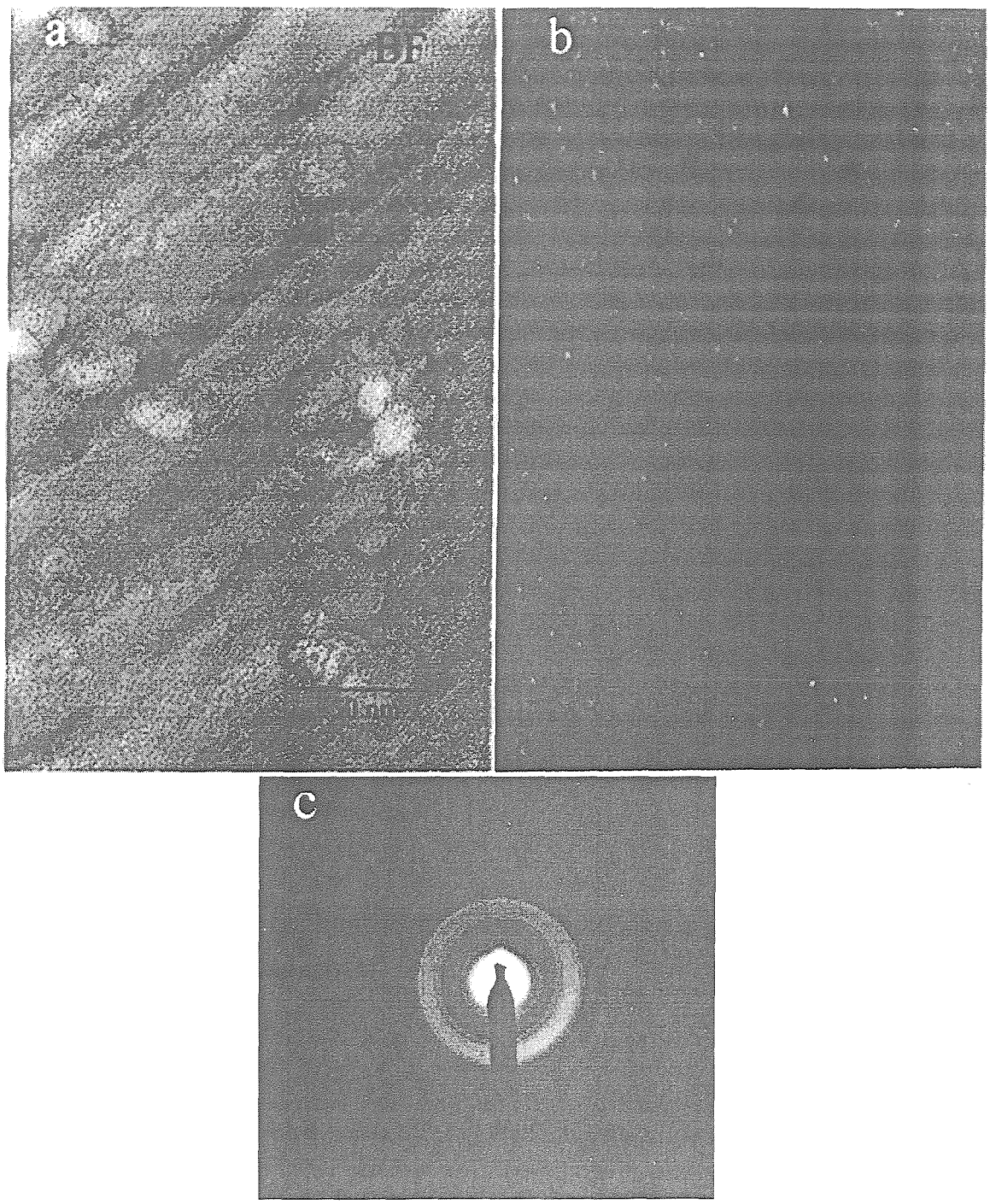

Fig. 5.3 (a)Bright-field, (b)dark field, and (c)selected area diffraction patterns TEM images of splat-quenched $Mg_{62}Cu_{25}Y_{10}Li_3$ sample annealed at 135 °C for 60 min.

Fig. 5.4 High resolution electron micrograph of splat-quenched $Mg_{62}Cu_{25}Y_{10}Li_3$ sample annealed at 135 °C for 60 min.

lighter contrast does not come from the thickness difference. This suggests the lighter region is different phase from the matrix. A high resolution TEM graph of the sample is shown in Fig. 5.4. One can see there are lighter and darker regions overlapping each other and some smaller groups of crystal fringes inside those regions, which is very similar to the TEM result of the bulk sample shown in Chapter 2. Here since the TEM sample sections are not thin enough and the lighter and darker domains are overlapping, it is hard to see if the crystal particles are within one type of the phase separated domains as seen in the case of the bulk samples.

Fig. 5.5 shows the small angle x-ray scattering intensity data of an as-prepared sample and of samples after annealing at 135 °C for different times. The as-prepared sample shows a strong small angle scattering which means that inhomogeneities already exist in it. The sample annealed for 30 min shows an increase in scattering intensity. For samples annealed for longer times, the scattering intensity increases with annealing time. A Guinier plot (ln(I) vs. q^2) [4] is shown in Fig. 5.6. The data analysis reveals the apparent radius of gyration (R_g) increases from about 50 to 90 Å with annealing time. When a crystal of differing composition nucleates in an otherwise homogeneous matrix, one expects the growth of the crystal to be limited by chemical diffusion. Such diffusion limited growth is expected to follow a growth law of the form $R \sim t^{1/2}$ where R is the average crystal radius and t is the elapsed time. The crystal is surrounded by a compositionally altered zone. The

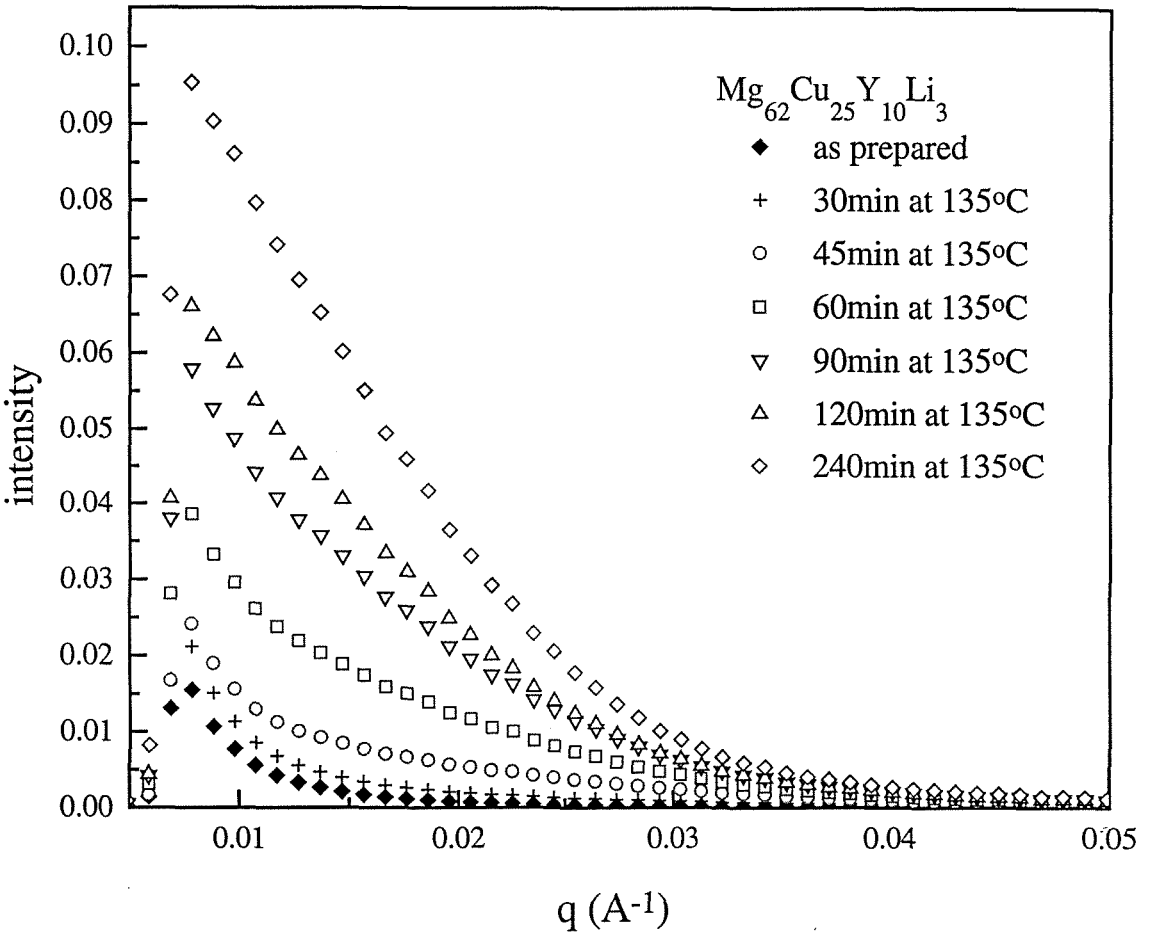

Fig. 5.5 Small angle x-ray scattering intensity data of an as-prepared splat-quenched $Mg_{62}Cu_{25}Y_{10}Li_3$ and of samples after annealing at 135 °C for different times.

crystal growth rate may fall below that predicted by the above law if: (1) the crystal nucleates and grows into a compositionally inhomogeneous matrix where the crystal grows "against" the composition gradient, or (2) multiple crystals nucleate in a homogeneous matrix and the compositionally altered zones surrounding neighboring crystals mutually impinge. Both mechanisms lead to a rapid fall off in the expected growth rate. Fig. 5.7 shows a logarithmic plot of the apparent radius of gyration, R_g, as a function of time. A "$t^{1/2}$" dependence is seen during the early stages of growth. The growth rate subsequently falls rapidly leading to an apparent limiting value of R_g of about 90-100 Å. This limiting size can be attributed to one of the two mechanisms mentioned above. In case (1), the bcc nanocrystals nucleate in an already phase separated liquid within a phase separated domain of favorable composition. Subsequent growth is limited by the size of the favorable phase separated domain. Growth into a neighboring phase separated domain is suppressed due to the unfavorable composition. In case (2), the initial matrix is homogeneous and crystal growth is limited by impingement of the compositionally altered zones around neighboring crystals. For case (2), the crystalline phase comes to chemical equilibrium with a matrix of differing but ultimately uniform composition, i.e., one achieves two-phase chemical equilibrium. Based on the high resolution TEM studies, we believe that the phase separation of the undercooled liquid precedes nucleation of the bcc nanocrystals. The TEM studies show that nanocrystallites of the bcc phase nucleate within one of the two types of phase separated domains. This evidence favors interpretation of the present data according to case (1) above.

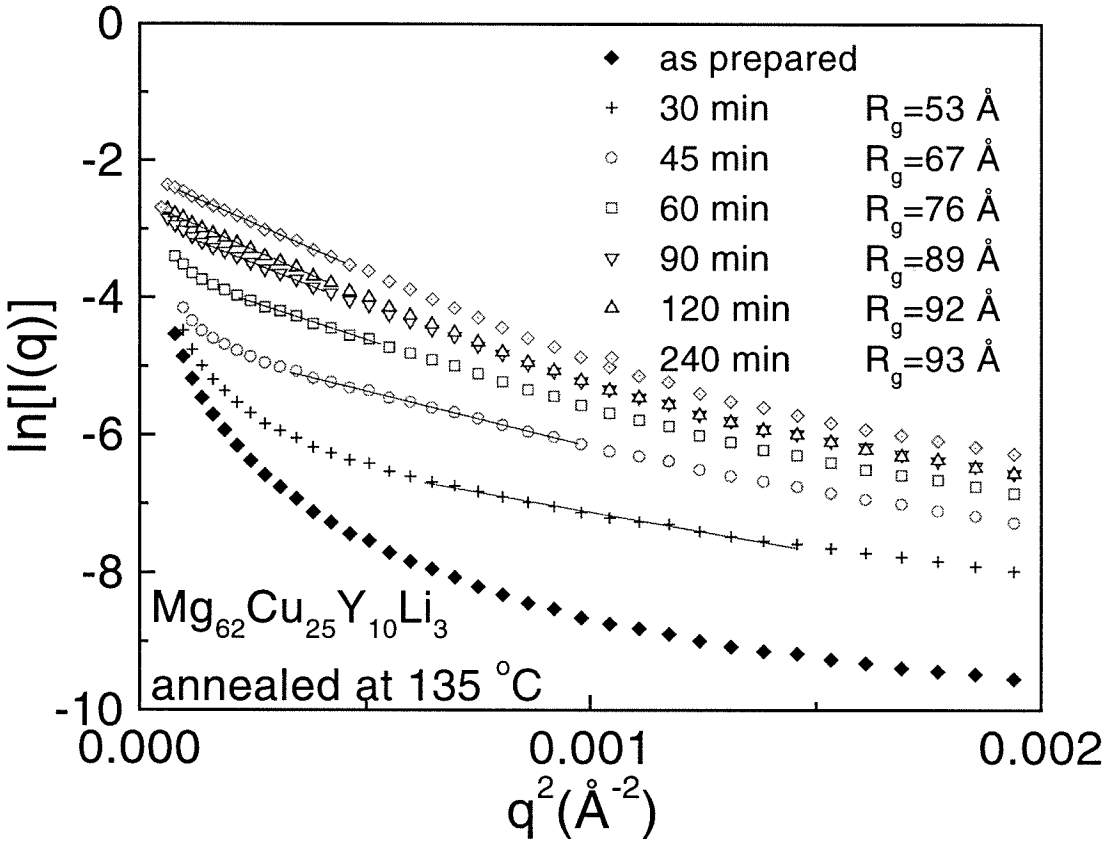

Fig. 5.6 Guinier plots of the small angle scattering intensity data of an as-prepared splat-quenched $Mg_{62}Cu_{25}Y_{10}Li_3$ and of samples after annealing at 135 °C for different times.

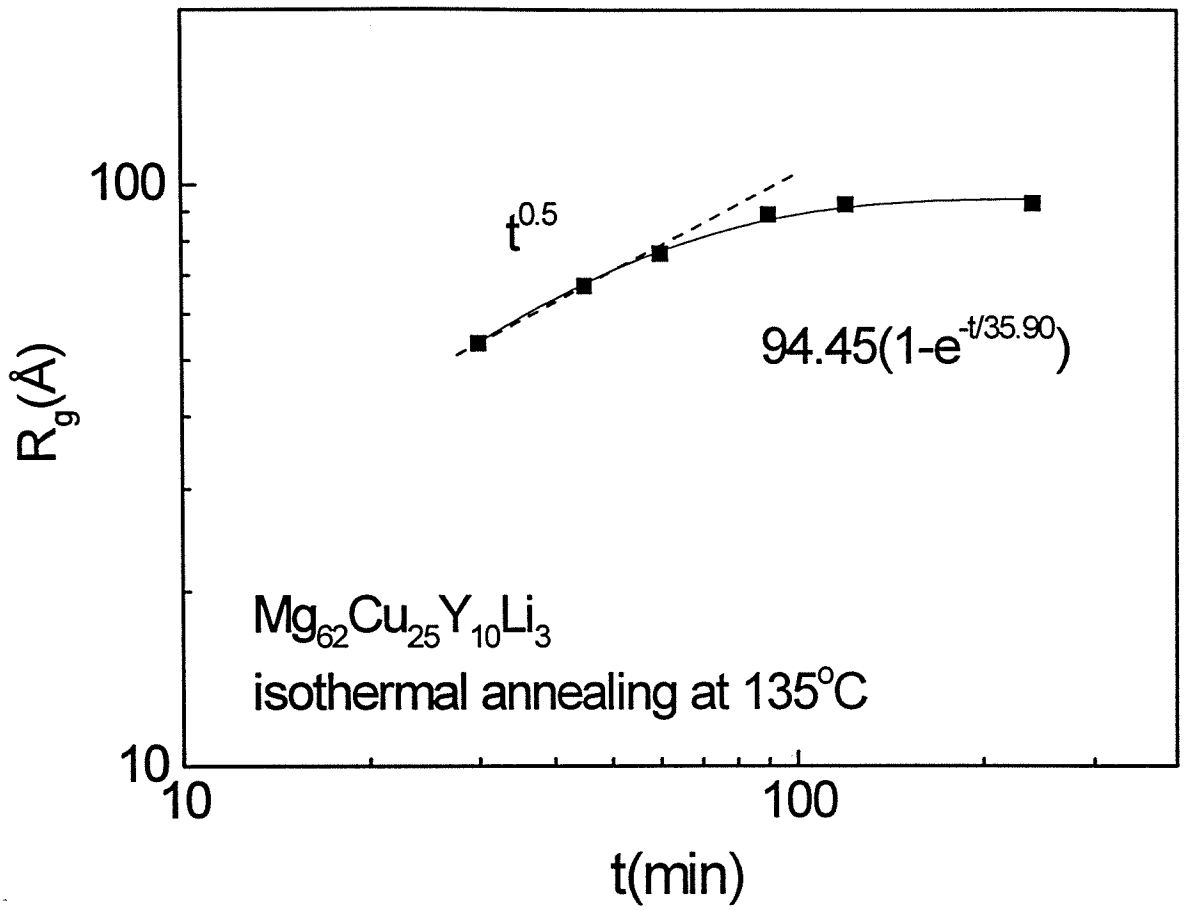

Fig. 5.7 Annealing time dependence of the apparent radius of gyration R_g for $Mg_{62}Cu_{25}Y_{10}Li_3$ samples aged at 135 °C.

According to Porod's law of small angle scattering [5], the final slope of log(I) vs. log(q) at large q range where $q \cdot R_g >> 1$ gives information on the interface between matrix and particles. If there exists a sharp interface, the scattering intensity follows a q^{-4} law, while a diffuse or rough interface will exhibit a power law in the scattering intensity with respect to q with an exponent in the range of -3 to -4, depending on the roughness. The double logarithmic plot of the scattering intensity is shown in Fig. 5.8. One can see that the slope for the as-prepared sample is close to -3. After annealing, the slope increases with annealing time and gets closer to -4. This suggests that the as-prepared sample has a diffuse interface between the phase separation domains. During heat treatment, the nanocrystals nucleate and grow. The crystals growth is restricted probably due to the fact that the subsequent growth of these nanocrystals would be limited by the size of the phase separation domains since there is a composition difference. Thus, the phase separation apparently limits the growth of the crystals while the crystal growth sharpens the boundaries of the phase separation.

Anomalous small angle x-ray scattering (ASAXS) [6, 7, 8] refers to extension of standard SAXS experiments in which the energy of the probing x-rays are tuned near the absorption edge of an element in the sample. By performing SAXS experiments near the characteristic absorption edge of any given atom, it is possible to vary the contrast for scattering of that particular element. Fig. 5.9 shows the ASAXS data of $Mg_{62}Cu_{25}Y_{10}Li_3$ annealed for 120 min at 135 °C around the Cu absorption edge. The ASAXS data were collected at 8776, 8940, 8969, and 8973 eV.

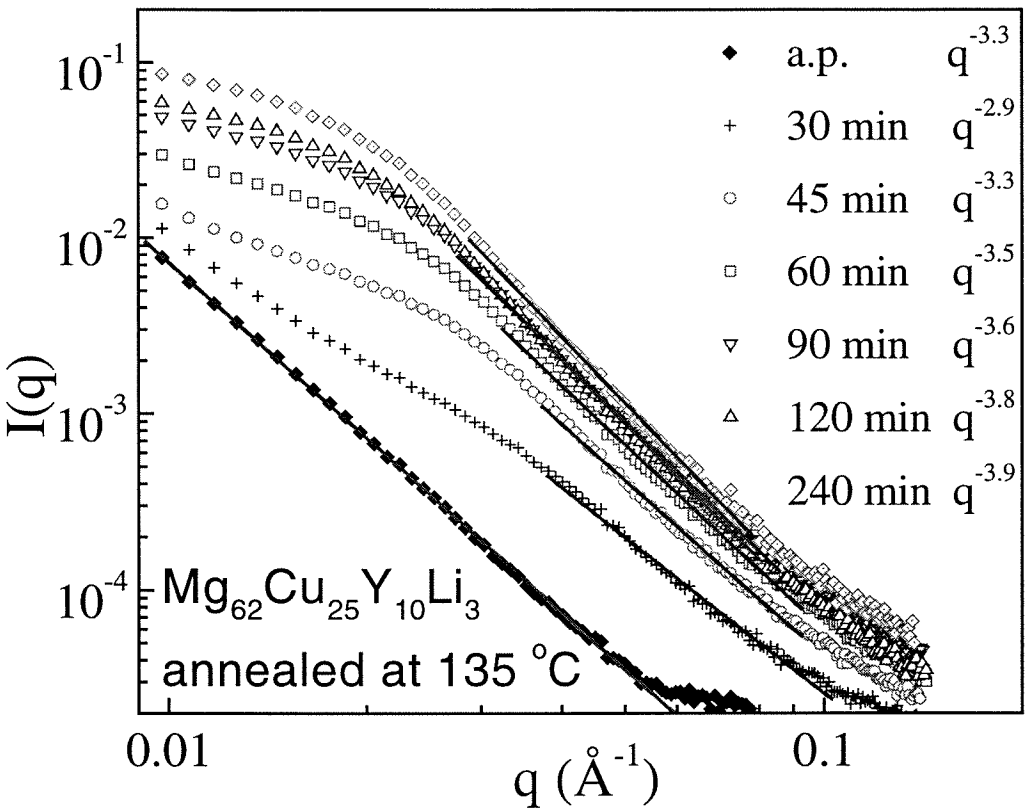

Fig. 5.8 Double logarithmic plots of the SAXS data of $Mg_{62}Cu_{25}Y_{10}Li_3$ annealed at 135 °C for different times.

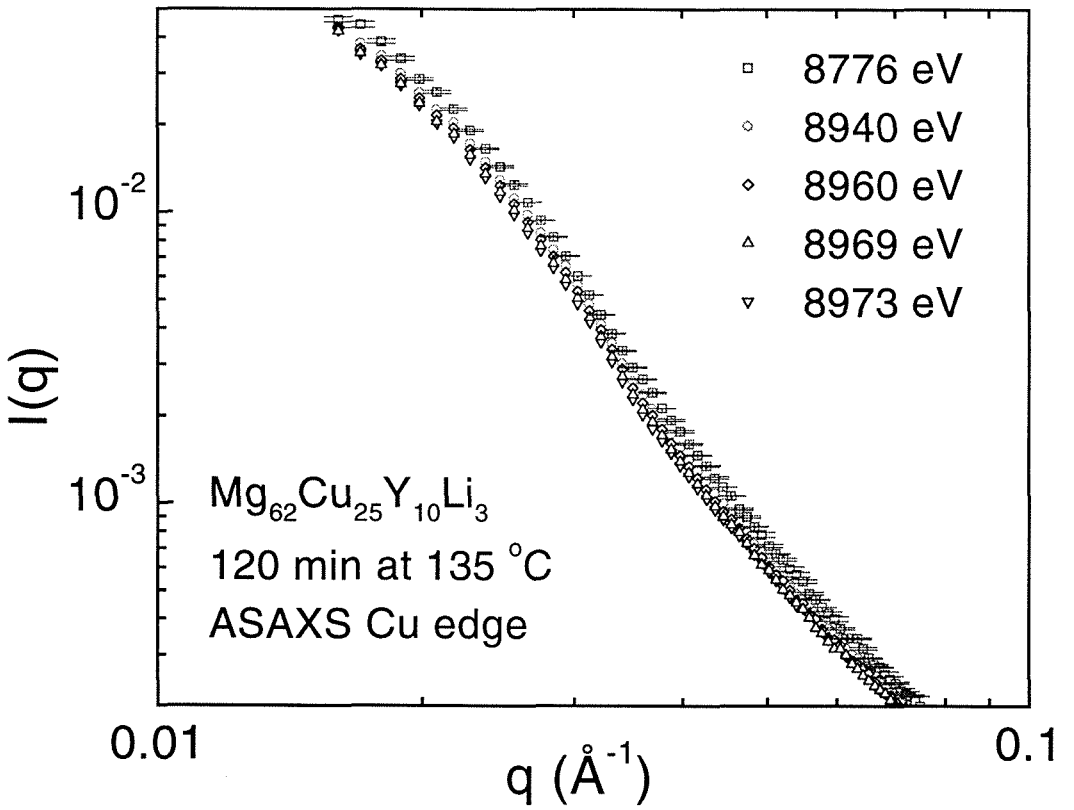

Fig. 5.9 The anomalous small angle x-ray scattering near Cu absorption edge of $Mg_{62}Cu_{25}Y_{10}Li_3$ after annealing 120 min at 135 °C. The lowest energy (8776 eV) is well below the Cu K edge (8979 eV), all others are near the absorption edge. The error bars are very small and hence are shown only for the curve measured at 8776 eV.

The lowest energy is well below the Cu K edge (8979 eV) while all others are near the absorption edge. Fig. 5.9 shows that the scattering intensity decreases as the x-ray photon energy increases towards the absorption edge. This implies that the alloy decomposes into Cu-rich and Cu-poor domains. It is known that for the Mg-Cu-Y amorphous system the glass transition temperature increases with increasing Cu concentration. Hence, the crystallization should preferentially start in the Cu-poor domains since the Cu-poor domains are thermally less stable with respect to crystallization than the Cu-rich ones. Further growth of these crystals should be limited by the size of phase separation domains. This is consistent with the fact that the crystallization of this alloy occurs first into a Mg-Li-rich nanocrystalline phase embedded in a Cu-rich amorphous matrix.

To investigate the bulk cast samples, we used small angle neutron scattering (SANS) since the SAXS experiments require very thin samples to get enough scattering intensity while the cast strips are suitable for SANS. Fig. 5.10 shows the small angle neutron scattering intensity data of an as-prepared cast specimen of $Mg_{62}Cu_{25}Y_{10}Li_3$ and of similar samples after annealing at 135 °C for 60 and 120 min. The scattering intensities of the annealed samples increase only slightly from the as-prepared sample and there is almost no difference between annealed samples for the two different times. The Porod plots of the SANS data are shown in Fig. 5.11. For the as-prepared sample, the slope is 3.62 and for the annealed samples the slopes become somewhat higher, which means that the interface of the as-prepared sample is already relatively sharp with the heat treatment sharpens the interfaces a bit more.

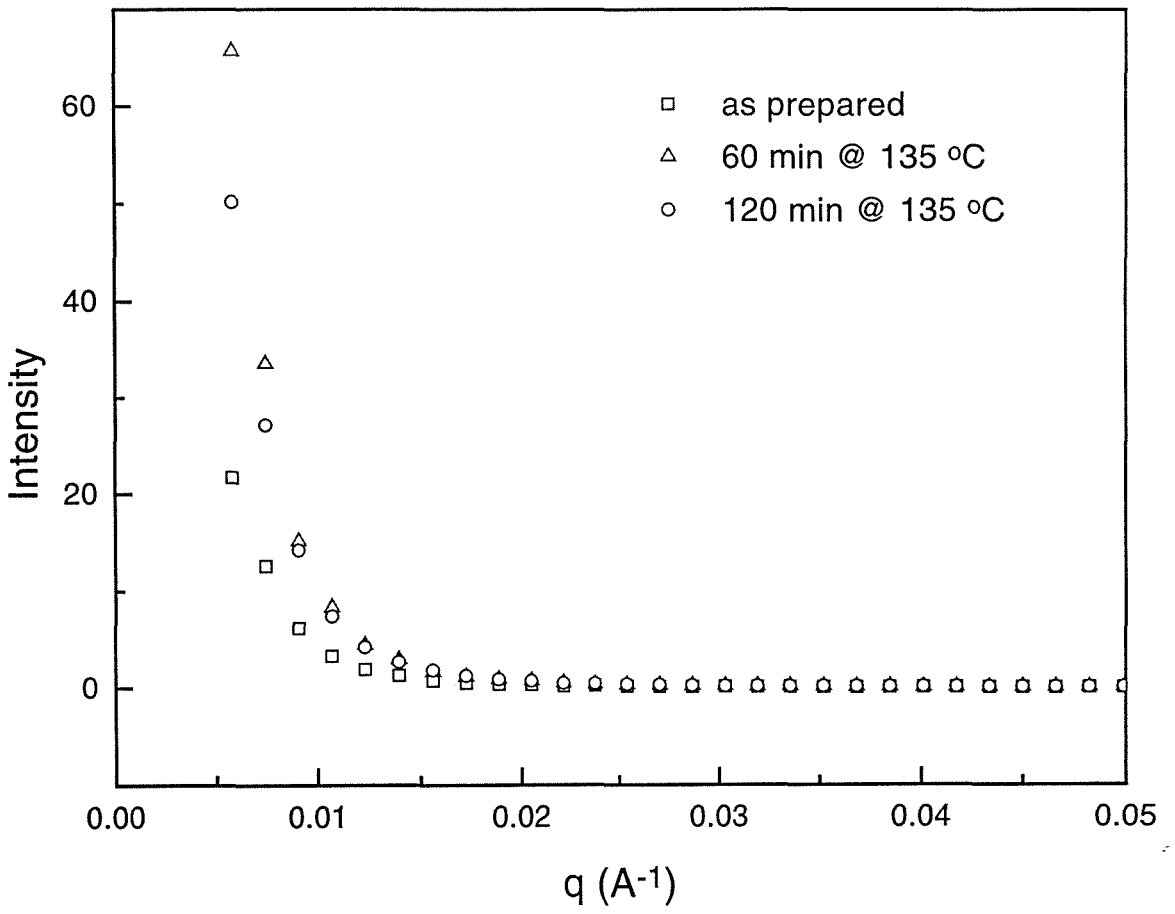

Fig. 5.10 Small angle neutron scattering intensity data of an as prepared casting $Mg_{62}Cu_{25}Y_{10}Li_3$ and of samples after annealing at 135 °C for 60 and 120 min.

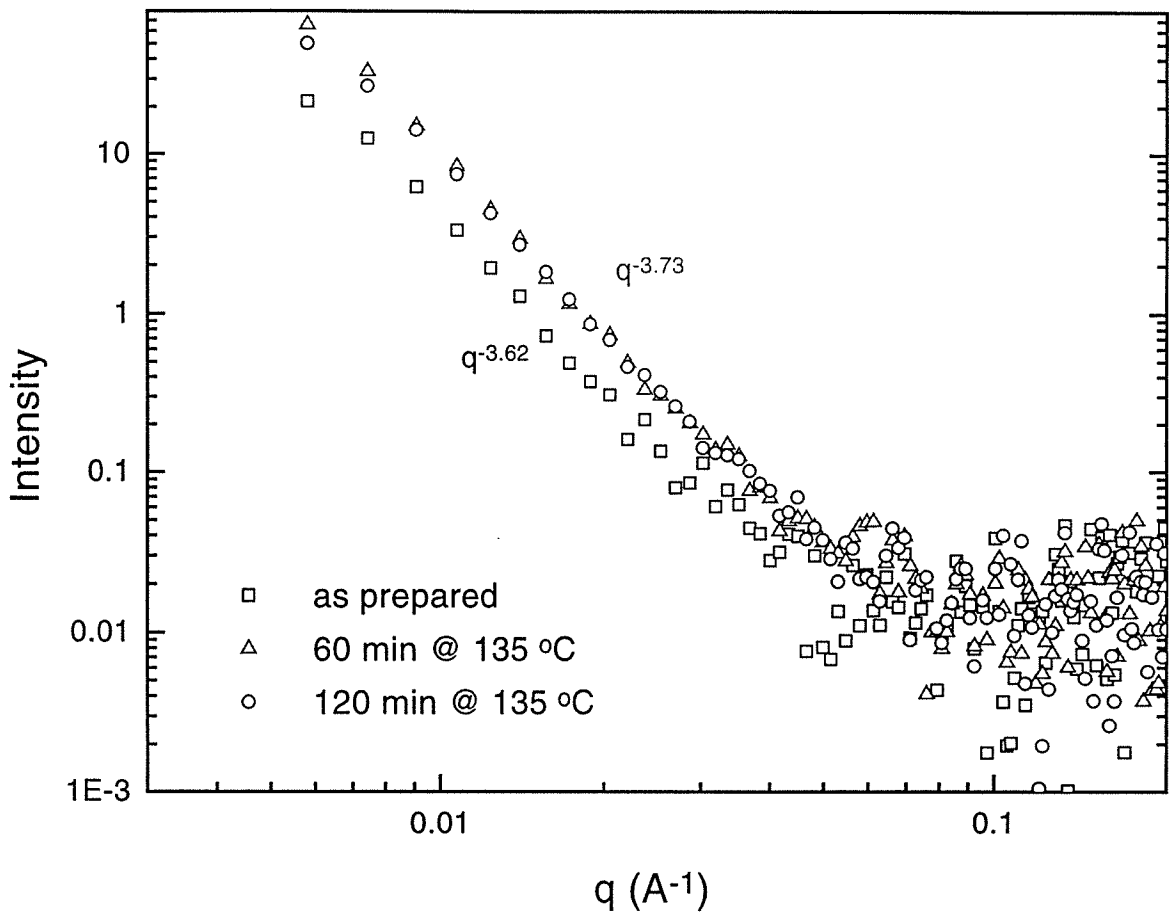

Fig. 5.11 Double logarithmic plots of the SANS data of $Mg_{62}Cu_{25}Y_{10}Li_3$ annealed at 135 °C for 60 and 120 min.

Since these samples were cast in bulk (with 1 mm thickness) and have a slower cooling rate (10^3 K/s) compare to the splat-quenched samples (10^6 K/s). The SANS results suggest that the samples prepared by casting are at the "later" stages of decomposition and already contain nanocrystals in an amorphous matrix. The annealing which occurs during casting makes the crystals grow bigger and sharpens the interface. This is consistent with the TEM images of the casting samples.

5.3 Conclusion

Phase separation and crystallization of $Mg_{62}Cu_{25}Y_{10}Li_3$ alloy were studied. It is observed that phase separation exists in the as-prepared splat-quenched sample. Nanocrystals nucleate and grow during annealing at 135 °C for about 30 min and reach a size of about 50 to 90 Å. The interfaces of phase separation domains are rough in the as-prepared state and become sharper with annealing time. ASAXS investigations showed inhomogeneities in Cu concentration. From the above, we conclude that the $Mg_{62}Cu_{25}Y_{10}Li_3$ alloy decomposes during cooling in the liquid state and forms a two-phase mixture of respective Cu-rich and Cu-poor amorphous domains. After heat treatment, the crystallization begins in the Cu-poor domains which are thermally less stable. Further growth of these crystals is restricted by the boundaries of the phase separation domains and hence sharpens the boundaries. Since nanocrystals are observed in as-prepared bulk samples of $Mg_{62}Cu_{25}Y_{10}Li_3$

prepared at a cooling rate of about 10^3 K/s, the critical rate for crystallization must be higher than 10^3 K/s.

REFERENCES

[1] P. Duwez, Trans. AMS, **60**, 609 (1967).

[2] S. Wakatsuki, K. O. Hodgson, D. Eliezer, M. Rice, S. Hubbard, N. Gills, S. Doniach, and U. Spann, Rev. Sci. Instrum., **63**, 1736 (1992).

[3] W. Liu and W. L. Johnson, J. Mater. Res., **11**(9), 2388 (1996).

[4] A. Guinier and G. Fournet, *Small-Angle Scattering of X-rays*, (John Wiley, New York, 1955), p126-160.

[5] O. Glatter and O. Kratky, *Small Angle X-ray Scattering*, (Academic Press, London, 1982), p27-50, p456.

[6] H. B. Stuhrmann, Quarterly Rev. Biophys, **14**, 433 (1981).

[7] J. E. Epperson and P. Thiyagarajan, J. Appl. Cryst., **21**, 652 (1988).

[8] P. Thiyagarajan, K. A. Carrado, S. R. Wasserman, K. Song, and R. E. Winans, Rev. Sci. Instrum., **67**, 1 (1996).